Geochemistry, Geophysics, Geosystems

RESEARCH ARTICLE
10.1029/2024GC011629

Special Collection:
Advances in understanding volcanic processes

How Did Westward Volcaniclastic Deposits Accumulate in the Deep Sea Following the January 2022 Eruption of Hunga Volcano?

Marcus Chaknova[1,2], Thomas Giachetti[1], Joali Paredes-Mariño[3], Adam Soule[4], Alexa R. Van Eaton[5], Roxanne Beinart[4], Martin Crundwell[6], Shane J. Cronin[3], Martin Jutzeler[7], Kristen E. Fauria[8,9], Michael A. Clare[10], Isobel A. Yeo[10], Shawn Arellano[11], Liam Kelly[8], Sally Watson[12,13], Rebecca Carey[7], Taaniela Kula[14], and Craig M. Young[2]

[1]Department of Earth Sciences, University of Oregon, Eugene, OR, USA, [2]Oregon Institute of Marine Biology, University of Oregon, Eugene, OR, USA, [3]School of Environment, University of Auckland, Auckland, New Zealand, [4]Graduate School of Oceanography, University of Rhode Island, Kingston, RI, USA, [5]U.S. Geological Survey, Cascades Volcano Observatory, Vancouver, WA, USA, [6]GNS Science Te Pu Ao, Lower Hutt, New Zealand, [7]School of Natural Sciences and Centre for Ore Deposit and Earth Sciences (CODES), University of Tasmania, Hobart, TAS, Australia, [8]Department of Earth and Environmental Sciences, Vanderbilt University, Nashville, TN, USA, [9]National Energy Technology Laboratory, Albany, OR, USA, [10]Ocean BioGeoscience, National Oceanography Centre, Southampton, UK, [11]Biology Department, Western Washington University, Bellingham, WA, USA, [12]National Institute of Water and Atmospheric Research, Wellington, New Zealand, [13]Institute of Marine Science, University of Auckland, Auckland, New Zealand, [14]Tonga Geological Services, Government of the Kingdom of Tonga, Nukualofa, Tonga

Marcus Chaknova and Thomas Giachetti contributed equally.

Key Points:

- Extensive volcaniclastic deposits sourced from the 15 January 2022 eruption of Hunga volcano were found >100 km away from the source
- The presence of foraminifera and radiolaria reveals erosional dynamics of volcaniclastic submarine density currents
- Long runout submarine density currents reached erosional threshold 80 km away from the source

Supporting Information:

Supporting Information may be found in the online version of this article.

Correspondence to:

M. Chaknova,
mchaknov@uoregon.edu

Citation:

Chaknova, M., Giachetti, T., Paredes-Mariño, J., Soule, A., Van Eaton, A. R., Beinart, R., et al. (2025). How did westward volcaniclastic deposits accumulate in the deep sea following the January 2022 eruption of Hunga volcano? *Geochemistry, Geophysics, Geosystems*, *26*, e2024GC011629. https://doi.org/10.1029/2024GC011629

Received 26 APR 2024
Accepted 2 MAR 2025

Author Contributions:

Conceptualization: Thomas Giachetti
Data curation: Martin Crundwell

Abstract

Most volcanic eruptions on Earth take place below the ocean surface and remain largely unobserved. Reconstruction of past submerged eruptions has thus primarily been based on the study of seafloor deposits. Rarely before the 15 January 2022 eruption of Hunga volcano (Kingdom of Tonga) have we been able to categorically link deep-sea deposits to a specific volcanic source. This eruption was the largest in the modern satellite era, producing a 58-km-tall plume, a 20-m high tsunami, and a pressure wave that propagated around the world. The eruption induced the fastest submarine density currents ever measured, which destroyed submarine telecommunication cables and traveled at least 85 km to the west to the neighboring Lau Basin. Here we report findings from a series of remotely operated vehicle dives conducted 4 months after the eruption along the Eastern Lau Spreading Center-Valu Fa Ridge. Hunga-sourced volcaniclastic deposits 7–150 cm in thickness were found at nine sites, and collected. Study of the internal structure, grain size, componentry, glass chemistry, and microfossil assemblages of the cores show that these deposits are the distal portions of at least two ∼100-km-runout submarine density currents. We identify distinct physical characteristics of entrained microfossils that demonstrate the dynamics and pathways of the density currents. Microfossil evidence suggests that even the distal parts of the currents were erosive, remobilizing microfossil-concentrated sediments across the Lau Basin. Remobilization by volcaniclastic submarine density currents may thus play a greater role in carbon transport into deep sea basins than previously thought.

Plain Language Summary

A large portion of Earths volcanic record is undiscovered in deep sea sediments. Few deep-sea volcanic deposits have a known volcanic source. Identifying the source of submarine volcanic deposits is crucial for understanding global carbon and iron cycles. The 15 January 2022 eruption of Hunga volcano, Kingdom of Tonga was the largest volcanic eruption observed in the modern satellite era. It produced a record setting volcanic plume sending volcanic ash and water 58 km into the atmosphere. Below the ocean's surface, fast traveling (∼122 km/hr) submarine landslides known as submarine density currents eroded the seafloor and destroyed submarine tele-communication cables. We discovered meter-thick volcanic deposits from this eruption, 80–100 km West of the volcano. In order to understand the source and transport of these deposits, we examined their chemical composition, grain-sizes and microfossils contained within them. Microfossils comprising shells of plankton were used to define signatures of erosion and transport of fauna in the submarine density currents. We discovered that these submarine density currents are erosive enough to move carbon-rich sediments from one place to another; this may play a pivotal role in global carbon and iron cycles in the deep sea.

Formal analysis: Thomas Giachetti, Joali Paredes-Mariño, Alexa R. Van Eaton, Martin Crundwell
Funding acquisition: Craig M. Young
Investigation: Thomas Giachetti, Taaniela Kula
Methodology: Thomas Giachetti, Joali Paredes-Mariño, Alexa R. Van Eaton, Roxanne Beinart, Martin Crundwell
Project administration: Craig M. Young
Supervision: Thomas Giachetti, Roxanne Beinart, Shawn Arellano, Craig M. Young
Writing – original draft: Thomas Giachetti, Joali Paredes-Mariño
Writing – review & editing: Thomas Giachetti, Joali Paredes-Mariño, Alexa R. Van Eaton, Roxanne Beinart, Shane J. Cronin, Martin Jutzeler, Kristen E. Fauria, Michael A. Clare, Isobel A. Yeo, Shawn Arellano, Liam Kelly, Sally Watson, Rebecca Carey

1. Introduction

Most volcanoes on Earth lie beneath the ocean surface and remain largely unobserved (Crisp, 1984; Sigurdsson, 2015). Over 119 submarine eruptions since 1913 have been detected via seismo-acoustics alone (Tepp & Dziak, 2021). In remote seas equipped with limited hydroacoustic and seismic sensors, deep-sea eruptions often go unnoticed unless they produce observable surface signals such as pumice rafts, discolored water, or volcanic plumes (Fauria et al., 2023; Jutzeler et al., 2014; Kelly et al., 2024; Olivé Abelló et al., 2021). Shallow water volcanoes present a unique set of challenges, with potential eruption or earthquake induced impacts on both the terrestrial and submarine realms. Interactions between magma and water can produce explosive volcanic plumes transporting aerosols and particulates high into the atmosphere (Fauria et al., 2023; Proud et al., 2022). Coastal communities may be impacted by eruption-triggered tsunamis, pumice rafts and/or volcanic ash fallout (Lynett et al., 2022; Ohno et al., 2022). Furthermore, eruption-fed density currents at shallow water volcanoes pose a major risk to submarine telecommunication networks that host ~95% of global digital data traffic (Burnett & Carter, 2017; Carter et al., 2015; Pope et al., 2017). These impacts call for a better understanding of how shallow submarine eruptions unfold and an improved identification of the hazards shallow water volcanoes pose.

Although submarine volcanic eruptions are mostly undocumented, there are several examples where they have measured impacts on ecosystems, people, and infrastructure. In 2011, the shallow water eruption of Tagoro volcano, off the southern coast of the Canary Island of El Hierro in the Atlantic Ocean, led to a severe submarine deoxygenation event (−96% depletion in O_2), resulting in mass mortality of the ecosystem (González-Vega et al., 2022). In 2012, a 400 km^2 pumice raft was tracked to its source at Havre volcano in the south-west Pacific Ocean, leading to the discovery of the largest deep-sea silicic eruption ever recorded (Carey et al., 2014; Jutzeler et al., 2014). More recently, pumice rafts from the 2021 eruption of Fukutoku Okanoba, in the Bonin Islands of Japan clogged the harbors of Okinawa and Maejima, temporarily shutting down their marine industries (Fauria et al., 2023).

The traces left by submarine eruptions are used to reconstruct geological, oceanographic and climactic records, but rarely have we been able to link an observed high-magnitude eruption to their deep-sea deposits (Carey et al., 2014; Trofimovs et al., 2008; Wiesner et al., 1995). Widespread submarine volcanic deposits often signify important chronological markers (Pattan et al., 1999, 2001; Ponomareva et al., 2015), a fundamental tool beyond carbon-dating to understand climate change through time (Freundt et al., 2023). Accurate interpretation of submarine volcaniclastic deposits allows us to develop hazard catalogs of events that extend far beyond instrumental and historical records (Ercilla et al., 2021). With time, submarine deposits can lose fidelity due to erosion from subsequent mass flows, remobilization of sediments by bottom currents, compaction, bioturbation, and chemical alteration by seawater and hydrothermal fluids (Freundt et al., 2023; Wetzel, 2009). In highly active volcanic centers, subsequent erosive density currents can remove all evidence of a volcanic event, resulting in an incomplete volcanic record (Cassidy et al., 2014). Thus, a timely collection of submarine volcanic samples provides the best opportunity to produce a complete and precise interpretation of the submarine eruption (Baker et al., 2002; Baumberger et al., 2014; Carey et al., 2014; Deardorff et al., 2011; Embley et al., 2014; Hayward et al., 2022; Rubin & Macdougall, 1989; Somoza et al., 2017; Walker et al., 2019). The detection of submarine eruptions relative to their true frequency remains limited, and the ability to access deposits in the deep sea is often challenging (Carey & Schneider, 2011; Engwell et al., 2014; Ledbetter & Sparks, 1979; Sparks & Huang, 1980; Trofimovs et al., 2008; White et al., 2015).

The Tongan Tofua arc has a well-documented modern volcanic record, totaling 77 eruptions since 1774 (Global Volcanism Program, Smithsonian Institution, https://volcano.si.edu/). However, few eruptions in this region have been directly observed (Chadwhick et al., 2008; Metz et al., 2016; Resing et al., 2011). In January 2022, the record-breaking eruption of Hunga volcano produced a 58 km tall plume (Proud et al., 2022), ~13 m tall tsunami (Lynett et al., 2022), and a pressure wave that propagated around the world (Matoza et al., 2022). The collapse of massive columns of hot, dense gas and pyroclasts also produced submarine density currents of rapidly cooling volcanic ash that destroyed submarine telecommunication cables, traveling tens of kilometers across the seafloor at speeds of up to 122 km/hr (Clare et al., 2023; Seabrook et al., 2023). In April 2022, we sailed across the Pacific to the Lau Basin back-arc spreading center, 80–100 km West of the Hunga caldera and the Tofua arc. We discovered and collected extensive ash deposits (up to 150-cm thick slurries) blanketing the previously sediment-barren seabed more than 2.1 km below the sea surface (Beinart et al., 2024). Direct sampling soon after explosive submarine eruptions is rare and has largely been confined to areas within a few kilometers of the vent. Thus, our study is unique in that we sampled volcanic material nearly 100 km from the volcano only 4 months after the eruption.

Here we present a geochemical, sedimentological, and micropaleontological analysis of these fresh volcaniclastic seafloor deposits. We first show that the juvenile fraction of the collected deposit is unequivocally from the 15 January 2022, eruption of Hunga volcano by comparing the chemistry of the collected samples with that of ash and lapilli collected on land during that eruption. Previous work has shown that powerful submarine density currents were triggered when the Hunga volcano eruption plume rapidly collapsed into the ocean (Clare et al., 2023; Seabrook et al., 2023), but those studies are limited to deposits <85 km from the edifice to the southwest and only <30 km to the northwest. Hence, the runout distance and the fate of these currents remain unknown. Using their geochemical, sedimentological, and microfossil characteristics, we show that our deposits represent the distal portions of at least two very-long-runout submarine density currents, which were then capped by ashfall from the subaerial plume. Finally, we attempt to extract the respective pathways of these submarine density currents from the Tofua arc to the Lau Basin by comparing their bioclastic content with previously documented sediment compositions in the region.

1.1. The 15 January 2022, Eruption of Hunga Volcano

Eruptive activity at Hunga Volcano, Kingdom of Tonga, began on 19 December 2021, and ended with a climatic eruption on 15 January 2022 (Gupta et al., 2022). The eruption on 15 January 2022 dispersed volcanic material in both the subaerial and submarine environments. Specifically, the atmospheric plume ascended to 58 km and produced a fast-growing umbrella cloud (Van Eaton et al., 2023) that deposited centimeters of ashfall across the Kingdom of Tonga (Mastin et al., 2024). Episodic collapse of the eruption column led to large-scale submarine density currents that descended the submarine flanks of Hunga at speeds up to 122 km/h (Clare et al., 2023). A ~400 km wide discolored water patch was present around Hunga in the days following the 2022 eruption, and has been interpreted as both a chlorophyll bloom triggered by the eruption (Barone et al., 2022) and an area where volcanic particles concentrate in the upper meters of the water column (Kelly et al., 2024; Whiteside et al., 2023).

It is estimated that more than 20 times as much material was emplaced by submarine density currents (~10 km^3) compared to atmospheric ashfall (~0.5 km^3) (Mastin et al., 2024). Rapid entry of large volumes of pyroclastic material into the ocean produced volcaniclastic granular flows that locally eroded the flanks of the edifice within 10 km of the caldera rim (Clare et al., 2023; Seabrook et al., 2023). In contrast, our study focuses on deposit characteristics in the distal realm, between 80 and 100 km from the vent, and at locations where meter thick deposits were not expected, from 1.8 to 2.8 km below the surface of the Pacific Ocean.

1.2. The Lau Basin

The Lau back-arc basin is the fastest documented spreading center on Earth, producing a highly active system of hydrothermal vents and seafloor mafic volcanism (Schmid et al., 2020). It is sandwiched between the Tonga ridge to the East and the Lau Ridge to the West (Figure 1). The basin sits rather shallow with a mean depth of 2.3 km, all above the Carbonate Compensation Depth (CCD) (Yan et al., 2020). Due to the regional tectonic complexity, the Lau Basin is divided into three major tectonic settings: the Western Basin, the Eastern Basin, and the Tofua Arc, where Hunga volcano is located. Hunga-sourced deposits from this study are constrained within the Eastern Lau Spreading Center (ELSC), located from 80 to 100 km West of the Tofua arc (Figure 1). The average slope from Hunga volcano down into the Eastern basin is 1.4°. Along this Westward path, two major obstacles disrupt the rather consistent slope: proximal seamounts (800–1,000 m high) along the Tofua arc and accretionary crust along the Eastern border of the ELSC (100–300 m high). Further details of the Lau Basin regional settings, used throughout this paper, can be found in Figure 1.

A variety of deposits exist in the distal Eastern Lau Basin, encompassing a range of rheologies from coarse granular concentrated currents to more dilute, fines-rich density currents (Clare et al., 2023). Similar, and larger scale mass sedimentation events have been documented from sampling of late Miocene deposits by the Integrated Ocean Discovery Program (IODP) within the Western Lau Basin (Figure S1 in Supporting Information S1). These core deposits suggest that submarine density currents have consistently transported large quantities of coarse and fine material into the otherwise sediment-starved Lau Basin (Hawkins, 1995). Within the IODP core,

10.1029/2024GC011629

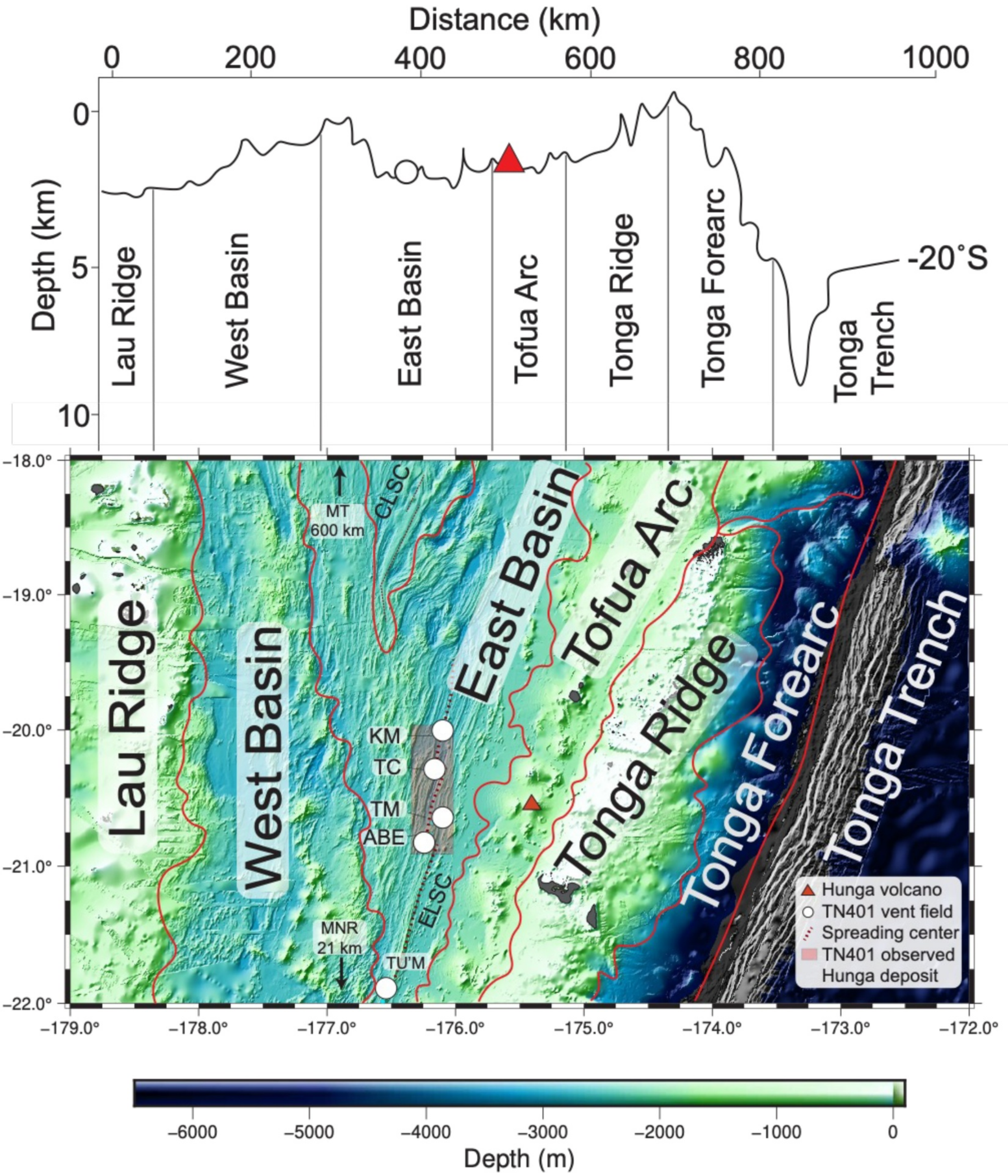

Figure 1. Bathymetric map showing the geological regional settings of the study. Bathymetry sourced by Ryan et al. (2009). Major geological settings labeled in large fonts are based on Stewart et al. (2022). Hydrothermal vent fields along the ELSC where TN401 was sampled (Table 1) are marked by white points. Hunga volcano is marked by a red triangle. The extent of the 2022-Hunga deposits observed during voyage TN401 is highlighted in orange. Off map are Mata Tolu, located 600 km to the North of the map, and Mariner vent field, located 21 km to the South of the map.

an average upward thinning of individual currents can be observed through the ~600-m thick deposit sequence from 23-cm to 59-cm. These density currents contain varying proportions of biological material (up to 15 vol.%) with a consistent calcareous composition (foraminifera, coccolithophore; Hawkins, 1995). Details surrounding how these deposits were emplaced are poor. Improved observations of recently emplaced submarine density currents with a known source can provide valuable insights into future studies of the Tonga arc volcanic record and the effects of pyroclastic influx into the deep-water Lau basin. This study builds on a framework to better interpret basin-filling deposits adjacent to volcanic arcs worldwide.

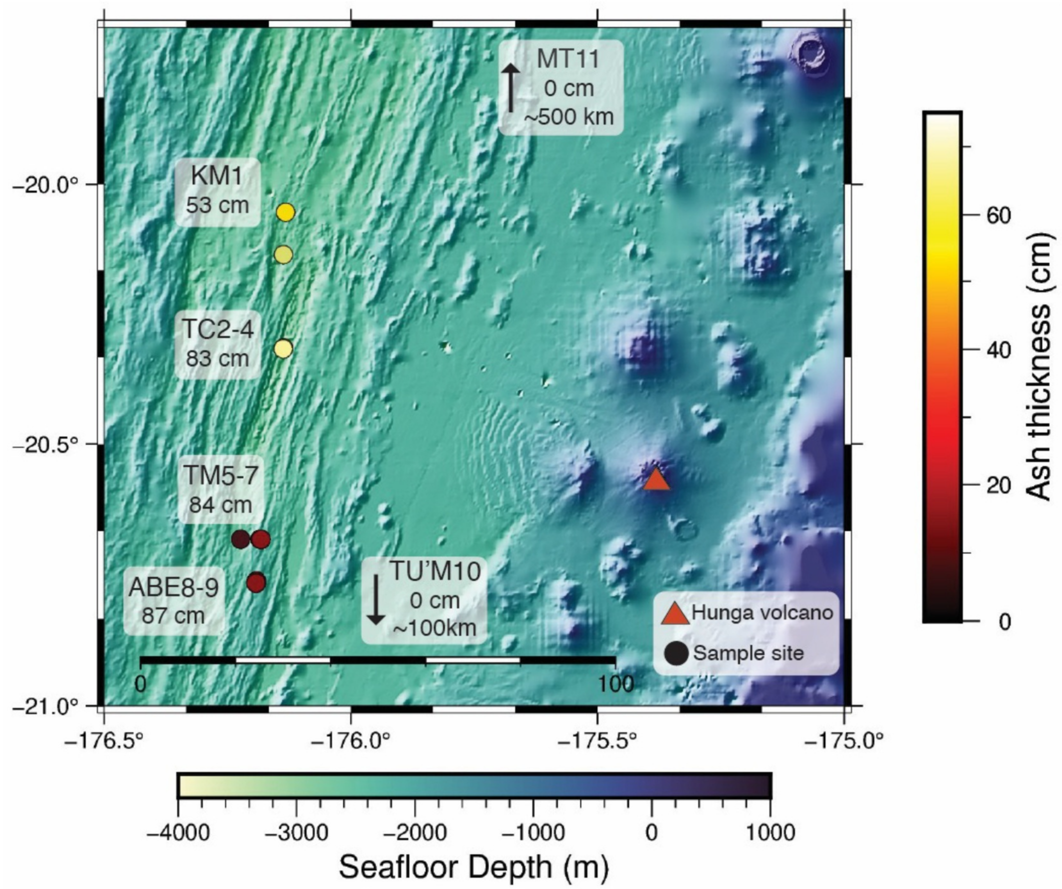

Figure 2. Samples within their respective vent fields (Table 1). Locations where samples were not collected due to the absence of deposits are also indicated. Color of points represents deposit thickness averaged over three measurements. Bathymetry sourced by Ryan et al. (2009).

2. Methods

2.1. Field

From April 3 to 27, 2022, remotely operated vehicle (ROV) *Jason* (National Deep Submergence Facility) dives were conducted from the R/V *Thomas G. Thompson* (University of Washington) on voyage TN401. Dives were carried out at five active hydrothermal vent fields and one inactive field along the Eastern Lau Spreading Center-Valu Fa Ridge in the Lau back-arc basin (Figure 2). The visited vent fields are located 83–222 km west of the Hunga volcano and range in depth from ∼1.8 to 2.8 km below the ocean surface. These hydrothermal vent fields have been observed many times (Du Preez & Fisher, 2018; Ferrini et al., 2008; Hodkinson & Cronan, 1998; Hourdez & Jollivet, 2018; Mottl et al., 2011; Sen et al., 2013). As of the most recent ROV dives in 2019 (Hourdez & Jollivet, 2018), none of these fields were covered by sediments. In April 2022, most were heavily sedimented.

ROV *Jason* was used to observe the seafloor at high spatial resolution and collect sediment samples using both scoop bags and push cores. We use the nomenclature *vent field abbreviation - sample #* (e.g., Kilo Moana, KM1) when identifying samples (Table 1). Except for our most Northern (MT-11) and Southern (TuM-10) sites that remained barren of sediment, the seafloor at these locations was always covered by up to 150 cm of newly deposited sediment when visited in April 2022 (Beinart et al., 2024).

We visited 11 sites across six vent fields and collected volcaniclastic deposits at all locations except for MT-11 and TuM-10 using either scoop bags or/and push cores (Figure 3). Smooth, flat deposit surfaces were chosen for collection to avoid potential discrepancies while measuring thickness on uneven substratum. Scooped samples

10.1029/2024GC011629

Table 1
Sample Identification, Vent Field, Coordinates and Associated Bathymetric Depth, Averaged Deposit Thickness (Beinart et al., 2024), Distance From Hunga Volcano and Remotely Operated Vehicle Collection Method

Sample	Vent field	Latitude	Longitude	Depth below surface (m)	Average deposit thickness (cm)	Distance from Hunga volcano (km)	Collection method
KM-1	Kilo Moana	−20.053656	−176.1322	2,630	53	96	Scoop
TC-2	Tow Cam	−20.31626	−176.13638	2,730	53	83	Scoop
TC-3	Tow Cam	−20.31785	−176.13721	2,720	63	83	Core
TC-4	Tow Cam	−20.317877	−176.13721	2,720	68	83	Scoop
TM-5	Tahi Moana	−20.682137	−176.18387	2,240	20	84	Scoop
TM-6	Tahi Moana	−20.682181	−176.1825	2,230	15	84	Core
TM-7	Tahi Moana	−20.682319	−176.18216	2,240	15	84	Scoop
ABE-8	ABE	−20.766029	−176.19203	2,150	15	87	Scoop
ABE-9	ABE	−20.765213	−176.19234	2,135	15	87	Scoop
TU'M-10	Tui Malila	−21.989167	−176.56767	1,870	0	201	N/A
MT-11	Mata Tolu	−15.0049	−173.7936	1,900	0	639	N/A

were taken from the seafloor to the top of the deposits and are not considered to have maintained deposit stratigraphy or to have sampled only the new deposit. Coring often required several attempts because the very fine material rarely remained suctioned within the core. Nine samples were successfully collected, including seven bagged samples and two cores (TC-3 and TM-6; Table 1). Sampling was limited due to difficulties in core retrieval and because these were samples of opportunity. Disturbances within sediment cores are a pivotal part of down-core interpretation (Jutzeler et al., 2014). Beds and contacts can deform upon collection, which requires accurate recognition to depict the undisturbed structure of the deposit. For example, an upper boundary is bent upward in core TM-6 by edge shearing between the core liner and the sediment. To minimize this edge effect, only the internal 3.5 cm of the core (laterally) was subsampled. Moreover, limited interpretations can be made of the top of this core due to liquefaction of the deposit during core retrieval. Similar cautions were taken in subsampling TC3 to avoid discrepancies due to coring disturbance.

Detailed methodology associated with the measurement of the deposit thickness is available in Beinart et al. (2024) together with the full list of deposit thicknesses (see their Table S2 in Supporting Information S1). Here, we discuss only average thicknesses (Table 1), which bear an estimated error of ±3 cm.

2.2. Computed Tomography

Push cores, TC-3 and TM-6, were CT-scanned on a Toshiba Aquilion 64 Slice Medical CT Scanner at the OSU College of Veterinary Medicine at 120 kV (200 mA), converted into 2-mm-thick coronal slices. The down-core and across-core pixel resolution within each slice is 500 μm. CT-Scans were performed to obtain a rough idea of the internal structure of the deposit.

Figure 3. Example of sediment sample collection by the remotely operated vehicle *Jason* at the Tow Cam vent field. (a) Deposit thickness measurement via a probe with 7.6 cm (3 inches) interval colored tape. (b) Canvas bag scoop method to collect mass material. (c) Push core retrieval of deposit.

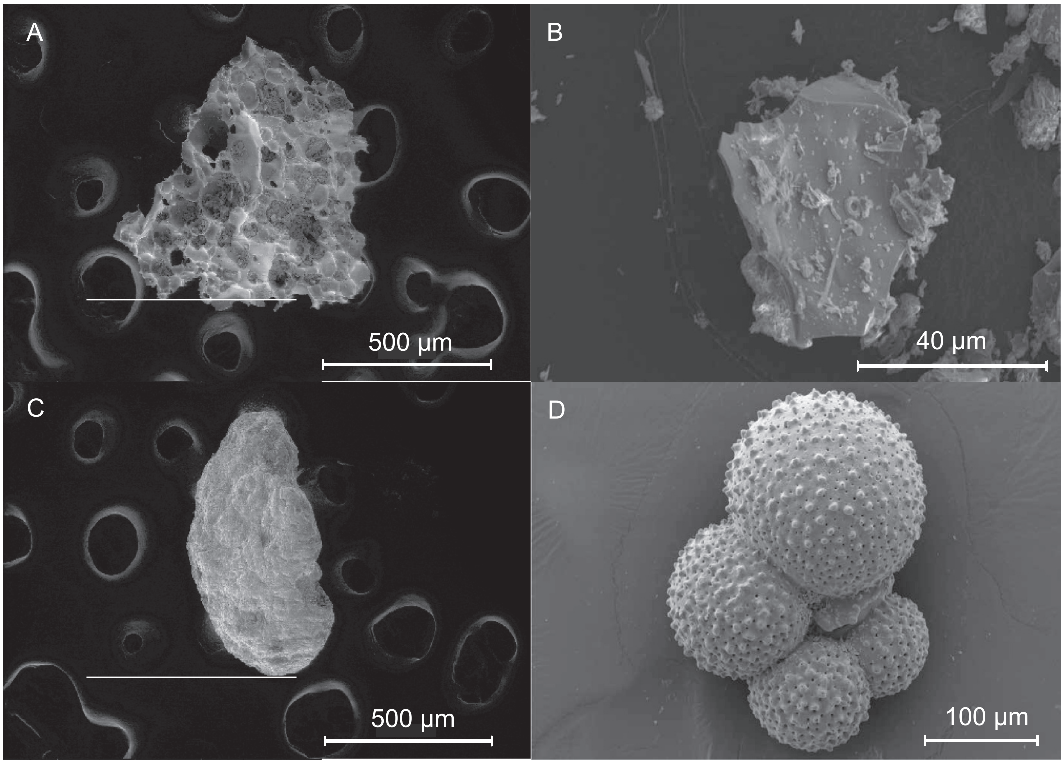

Figure 4. Scanning Electron Microscope imagery of components from core TM-6 at Tahi Moana, showing examples of each of the four main categories used in the componentry analysis. (a) Juvenile vesicular, (b) juvenile dense, (c) lithic clast, and (d) common planktonic foraminifera categorized as biological. Red rectangles in panel (b) highlight examples of abundant nannofossils (coccoliths and spines) within these deposits.

2.3. Grain Size Distribution and Density

Grain size distributions were obtained using laser diffraction using a Beckman Coulter LS 13 320 at the U.S. Geological Survey Cascade Volcano Observatory (WA, USA). This system only accepts particles <1 mm, which covers the vast majority of the particles in our samples. However, without analyzing the coarser fraction, we caution that the results only provide a relative grain size distribution for comparing among sites examined in this study. Each sample was analyzed three times for 60 s each time to produce an average size distribution of the material <1 mm. For the optical model, we used a refractive index of 1.56 and an absorption coefficient of 0.1, values that are commonly used for andesite ash (Horwell, 2007). Median grain size was determined as the 50th percentile on a plot of particle diameter versus cumulative volume percentage for each sample.

The density of the bulk sample was analyzed using a Micromeritics AccuPyc II 1340 pycnometer at the University of Oregon (OR, USA) with high purity helium as the working gas and on 0.2–1.2 cm^3 of ash, depending on the sample availability. Each sample was measured five times to provide an average and standard deviation.

2.4. Componentry

Componentry methodology was adapted from Ross et al. (2021). Representative splits of ∼200 particles were created for three particle size bins (32–63 μm, 63–125 μm, 125–500 μm) using a mini riffle sample splitter. All particles were categorized into four primary components: vesicular juvenile, dense juvenile, non-juvenile (lithics), and biological material (Figure 4). Juvenile particles were distinguished from non-juvenile particles based on their luster, coloration, smooth texture and lack of rounding (Ross et al., 2021). Biological material was further sorted into calcareous forms (benthic and planktonic foraminifera) and siliceous forms (radiolarians, phaeodarians, and diatoms; see Figure 5).

Particles 125–500 μm were sorted and counted solely using an optical microscope. Componentry of particles 32–63 μm and 63–125 μm was performed on Scanning Electron Microscope (SEM) images. A minimum

10.1029/2024GC011629

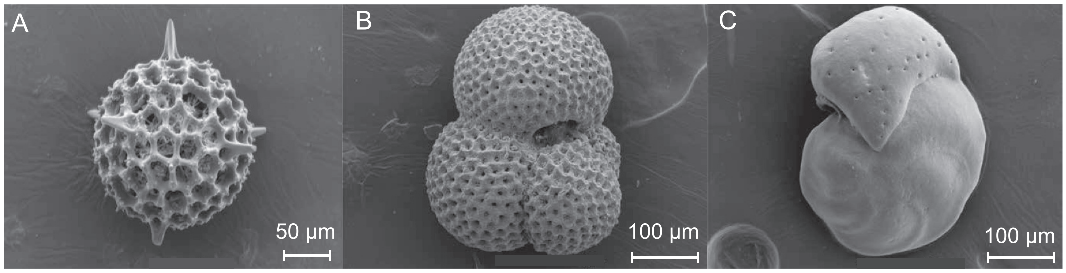

Figure 5. Scanning Electron Microscope imagery of biological components found in core TC-3 at the Tow Cam vent field described in Section 2.5.3. (a) Common spumellaria-polystina radiolarian found within deposits, (b) common planktonic-foraminifera, and (c) benthic foraminifera. The scale in panel (a) is 50 μm and it is 100 μm in panels (b, c).

magnification of 150 × (63–125 μm) and 300 × (32–63 μm) was maintained during the analysis. Both the SEM and the optical microscope were utilized for several 63–125 μm fractions to identify potential variability in componentry methods, but the two approaches gave similar results.

2.5. Micropaleontology

2.5.1. Sample Preparation

Each subsample from the cores was first dried at 70°C and then weighed. The subsample was then washed with water over a 63-μm mesh screen and disaggregated. Any material that was retained on the mesh screen was dried at 70°C. The washed and dried sample residues were then sieved into three size-fractions, where fossils were abundant (63–125 μm, 125–500 μm, and >500 μm), weighed and then transferred to small glass vials for micropaleontological examination.

2.5.2. Examination

Each washed residue was first examined under a stereomicroscope to determine the presence and abundance of foraminifera. When necessary, residues were subdivided with a microsplitter to obtain aliquots with 300–600 foraminifera. All foraminifera and ancillary microfossil material was picked and mounted onto 60-division microfossil slides. Mounted foraminiferan specimens and ancillary microfossil material in each sample were then identified, counted, documented for preservation state and composition of microfossil material, and key age and paleoenvironmental markers were recorded. Fragmented foraminifera (fragments and specimens <50% complete) were counted and converted to a standard fragmentation index (FI) based on Le and Shackleton (1992).

2.5.3. SEM Imaging and Taxonomy

Representative specimens from the horizon where foraminifera were most abundant (subunit 3 of TM-6, located 3–4 cm from the bottom of the core) were mounted in standard axial, umbilical, and spiral orientations for SEM imaging. The mounted specimens were gold coated and imaged using a JEOL JCM-6000 benchtop SEM. Phylogenetic classification for planktic foraminifera follows the schema of Aze et al. (2011) and Kennett et al. (1983). A Euclidean cluster analysis (PAST v.4.14 Software) was used to analyze the stratigraphic phylogenetic abundance of the foraminifera population.

2.6. Glass Geochemistry

To determine whether the juvenile fraction of the deposits collected in the Lau basin are from the 15 January 2022 eruption of Hunga volcano, ash particles were analyzed for major element concentrations and compared with terrestrial ash samples of that eruption collected a day after the eruption. Samples collected by scoop and by push core were sieved and individual grains were picked and mounted in epoxy. Exposed and polished grain surfaces ranged 10 μm–1 mm and displayed a range of porosity and crystallinity (Figure S7 in Supporting Information S1). Five to 15 grains were analyzed from each recovered sample along with grains (n = 37) from terrestrial ash deposits generated during the climactic phase of the 2022 Hunga eruption. Samples were analyzed by electron probe microanalyzer (EPMA) at Brown University. Each grain was analyzed at least twice to ensure consistency, and only in areas exhibiting crystal-free and vesicle-free clean glass. Samples were analyzed with a 15 kV, 10 nA, 10 μm wide defocused beam. Elements were measured for 30 s on peak and 15 s off peak (except Na, which is 20 and 10 s, respectively). Na and K were corrected using an element migration loss routine, and the glass compositions were calculated using PAP (Pouchou & Pichoir, 1991). Calibration standards with basaltic to andesitic compositions were measured before and after analysis sessions to correct for drift. Analyses with low (<96 wt.%) or high (>102 wt.%) totals were removed as they are interpreted to have inadvertently measured mineral phases or epoxy.

2.7. Smear Slides From Moorby et al. (1986)

The only published data quantitatively describing the micropaleontological compositions of the Lau Basin is from a former 1980s voyage of NZOI (now known as NIWA, the New Zealand National Institute of Water and Atmospheric Research). Because data from the NZOI voyage is incredibly useful to understand background sedimentation within the Lau Basin, we have refocused and digitized sediment smear slide data from the NZOI voyage to aid interpretation of the background microfossil and physical sediment compositions of the Lau Basin. Digitized raw data are presented in Table S6 in Supporting Information S1, while interpolated abundance and dispersion plots are refocused around Hunga and the ELSC and are presented in Figure 10.

3. Results

3.1. Extent and Thickness of the Ash Deposit

These hydrothermal vent fields have been observed many times (Du Preez & Fisher, 2018; Ferrini et al., 2008; Hodkinson & Cronan, 1998; Hourdez & Jollivet, 2018; Mottl et al., 2011; Sen et al., 2016). As of the most recent ROV dives in 2019 (Hourdez & Jollivet, 2018), none of these fields were covered by sediments. In April 2022, we found fresh deposits at all of the Lau Basin sites on which we dove (Figure 1, Table 1), except for our most Northern (Mata Tolu, MT-11) and Southern sites (Tui Malila, TuM-10). Dive sites covered an area ∼220 km long, 80–100 km west of the Hunga caldera. Thus, our observations demonstrate that the Hunga deposit covers an area far larger than that previously mapped by Seabrook et al. (2023). The deposits we measured ranged in thickness from 10 to 150 cm, with the thickest deposit (TC-4) being located 83 km north-west of Hunga volcano. We also identified the presence of ash deposits on laterally ejected flanges of hydrothermal vent chimneys up to ∼25 m above the ocean floor at the Tow cam vent field (Figure S2 in Supporting Information S1).

3.2. Stratigraphy of the Deposit

Cored samples preserve structures and thus provide more information on transport processes and sequence of events. For this reason, we focus our analyses on data from push cores (TM-6 and TC-3), while scoop sampled data is primarily confined to supplementary material (Figure S6 in Supporting Information S1). As explained in Section 3.2, both push cores TC-3 and TM-6 were split into sub-samples and results from these sub-samples allow us to distinguish five units within these cores based on sedimentological characteristics, grain size distribution (Figures S3 and S4 in Supporting Information S1), componentry, density of ash, and micropaleontology. TM-6 was found to comprise four potential units while TC-3 comprises a single unit. Below we describe the characteristics of each unit. Note that our probe-based thickness measurements suggest that TM-6 (10 cm thick) represents the entirety of the ash deposit at this location, whereas core TC-3 only represents the first 17 cm of a ∼63-cm-thick ash deposit.

3.2.1. Core Tahi Moana-6 (TM-6)

Core TM-6 represents the entire 10-cm thick volcaniclastic deposit with a median particle diameter that remains <50 μm throughout the whole core, although several coarser pumice clasts were identified that represent outliers (particles >5 mm at 3–4 cm and >1 mm at 6–7 cm below the deposit surface, respectively). All components described in Section 2.4 (vesicular juvenile, dense juvenile, lithic, microfossil) are present throughout the core but vary in proportion. Four depositional units are distinguished within this core (Figure 6). Boundaries between these units are not horizontal, which may be a product of deposition or produced by disturbance during sampling and transport. Due to the inclined nature of these contacts, thicknesses of the different units are thus given as a range at the center of the core, avoiding core edge disturbances. From the bottom (∼10 cm below the surface) to the top of the core (0 cm), we find: Unit-1, a 2 (±1)-cm thick unit with upward convex laminae; Unit-2, a 3(±1)-cm thick

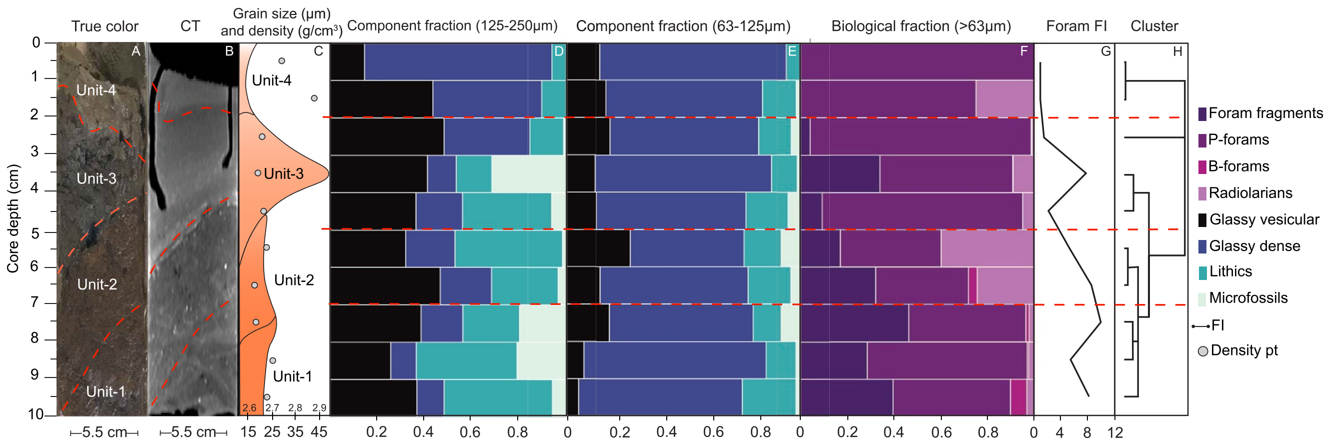

Figure 6. Description of core TM-6. From left to right: (a) true color imagery, (b) CT scan, (c) median grain size (shown as a curve) and bulk deposit density (shown as points), (d) componentry of particles 125–250 μm, (e) componentry of particles 63–125 μm, (f) biological componentry of all particles >63 μm, (g) fragmentation index of the forams, (h) euclidian cluster analysis of foraminifera.

structureless mud unit; Unit-3, a 3 (±1)-cm thick unit exhibiting parallel laminae; and Unit-4, a 1 (±0.5)-cm thick structureless, fine grained unit.

3.2.1.1. Basal Layer (Unit-1 and Unit-2)

The basal layer is composed of Unit-1 and Unit-2, characterized by an inversely graded base containing discontinuous lenticular laminae with a red/dark-brown coloration. It should be noted that due to poor scan quality and small core width, the primary structures (discontinuous laminae) cannot be distinctively distinguished from potential secondary structures (slump and/or shear). This layer is composed of silt-clay sized grains with some sand-sized foraminifera and a concentrated coarse lithic component relative to other units (15%–30% of 125–250 μm size fraction). The bioclastic content of the basal layer is unique to upper units by the presence of benthic foraminifera, and a large proportion of foraminifera fragments (up to 45% of the biological material). Units-1–2 are composed of 7% calcareous foraminifera and <1% siliceous radiolarians. Juvenile volcaniclastics in the finer size fractions (32–63 μm and 63–125 μm) represents the primary component (76%–89%) of the sediment throughout the layers, with a much higher proportion of dense to vesicular juvenile particles. At these smaller grain sizes, the proportion of lithics (11%–16%) and bioclastics (~8%) is lesser throughout the basal layer.

Unit-1 is structurally distinguished from Unit-2 by an inversely graded base with discontinuous laminae. It is further distinguished by a high bioclastic content (8%–20%) and low proportion of siliceous microfossils (<5%). The median grain diameter increases upwards in the unit from 23 to 28 μm. There is also an upward increase in the bioclastics from <6% to 20%. Fragmentation of foraminifera peaks at the boundary between Unit-1 and Unit-2.

In terms of biological population, Unit-1 exhibits a mix of encrusted (planktic foraminifera that have undergone gametogenesis and have either settled to the seafloor or are in the process of settling), crust-free, mostly smaller planktic foraminifera, and relatively common benthic foraminifera (~12%; Figure S5 in Supporting Information S1). The benthic assemblage includes bathyal species, but there are no diagnostic depth markers to determine the source of sediment. Euclidean cluster analysis separates the underlying Unit-1 from Unit-2 (see Figure 6h).

Unit-2 is distinguished by its bioclastic content and lack of structural features. The intersection of Units 1 and 2 is accompanied by a decrease in bioclasts (−15%) and a sharp increase in siliceous microfossils (+20%). Unit-2 presents normal grading, and a progressive upward decrease of the foraminiferal fragments (−30%). The bioclastic content is composed of mostly radiolarians, small encrusted planktic foraminifera and rare benthic foraminifera.

3.2.1.2. Unit-3

Unit-3 is structurally distinct from all other units with cm thick parallel laminae. At its base is a sharp <0.5 cm contact rich in sand-sized foraminifera clearly visible on the computed tomography data (Figure 6b). Laminations are composed of alternating bioclastic (light) and clay (dark) concentrated bands. Coarser bioclasts (125–250 μm) are concentrated to light colored laminae (>30% of coarsest size bin), while dark colored laminae are concentrated by clay. Juvenile volcaniclastics do not appear to follow a banding pattern (>90% of all size bins). The unit is on average composed of 8% calcareous foraminifera and <1% siliceous radiolarians. The componentry of particles <125 μm is similar between the basal layers (Unit-1 and Unit-2) and Unit-3. Cluster analysis separates the foraminifera population of the lower laminae of Unit-3 (3–5 cm) from the top laminae (2–3 cm).

3.2.1.3. *Unit-4*

The 1–2 cm layer atop core TM6 presents a break in laminae from Unit-3, forming a structureless, pale gray, fine-grained unit. This unit is the finest of all three units, with a gradual upward decrease of median particle diameter from its base (∼10 μm). Greater than 60 wt.% of Unit-4 is composed of extremely fine grains (<32 μm) compared to <50 wt.% for the underlying units. Unit-4 is characterized by a very high proportion (85%–90%) of coarse juvenile volcaniclastics in the 125–250 μm size fraction compared to the underlaying units. Bulk density is significantly increased in Unit-4, which is 5–20 (g/cm^3) denser than all other units. Unit-4 is composed of 2.5% calcareous foraminifera and <1% siliceous radiolarians. Bioclasts in Unit-4 are quasi absent in all size fractions (<4%) and, contrary to all underlying units, Unit-4 lacks fragments of foraminifera. The rare microfossils in Unit-4 are mostly small crust-free planktic foraminifera, very rare fish teeth, and corroded echinoid spines.

3.2.2. Core Tow Cam-3 (TC-3)

Based solely on visual observation of the core and computed tomography data, TC-3, which represents the top 17 cm of a ∼63-cm-thick volcaniclastic deposit, appears structureless and relatively homogenous in coloration and density (Figure 7). Grain size data show a normal grading (fining upward) throughout the core, with a median diameter (20–13 μm) decreasing upward. Componentry in the coarsest fraction (125–250 μm) shows a high proportion of juvenile volcaniclastics (68%–90%) made roughly of equal proportion of dense and vesicular material. One-cm-thick layers relatively rich in coarse (125–250 μm) bioclastics (20%–30%) are present 4–5 cm above the bottom and at the top of the core (0–1 cm). Except for these layers, coarse (125–250 μm) bioclastics are almost non-existent throughout the core (maximum <2%), the rest of the volume being made of lithic material (10%–31%). In the finer size fractions (63–125 μm), there is a high proportion of juvenile volcaniclastics throughout the core (62%–90%), with a much higher relative proportion of dense grains (42%–93%) compared to vesicular. Finer lithics are limited (4%–11%), and bioclastics range widely (1%–30%) within the smaller bin size. The highest concentration of biological material is located roughly midway through the core. TC-3 is composed of 12% siliceous radiolarians and >3% calcareous foraminifera. Grains <63 μm are primarily juvenile volcaniclastics (>87%, with >86% of it being dense material) with some lithic (∼7–10%), and a minor amount of bioclasts (<5%) with no noticeable change throughout the core. The bulk density of the material decreases up the core from ∼2.7 g/cm^3 to ∼2.6 g/cm^3.

3.2.3. Correlations Between the Two Cores

There are no obvious sedimentological correlations between core TC-3 and Units-1–4 seen in core TM-6. Core TC-3 is like Unit-4, such that both are structureless, light gray, fine-grained units poor in sand-sized bioclasts (125–250 μm). However, TC-3 is distinct from Unit-4 based on its high concentration of silt-sized bioclasts (63–125 μm), which is (>20% in TC-3 compared to <2% in Unit-4). The bioclastic composition is also dramatically different in TC-3. Bioclasts in TM-6 are foraminifera dominant (6%–7% of Units-1–3 compared to ∼3.4% of TC-3), while bioclasts in TC-3 are radiolarian dominant (12% of TC-3 compared to <1% of Unit-4 in TM-6), with foraminifera primarily constrained to 1-cm layers at 0–1 cm and 12–13 cm. Silt-sized foraminifera are more common at the base of TC-3 (30%–45% of the biological component at 1-cm intervals). For these reasons, we refer to the retained deposit of TC-3 as Unit-5 and refrain from making definite spatial correlations between units found in TC-3 and TM-6. Possible relationships between the two deposits are discussed in Section 4.2.

3.3. Geochemistry

Glass compositions were acquired by EPMA on grains from the cores (TC-3 and TM-6) and scoop samples, and on terrestrial ash samples collected by the Tongan Geological Services on Fonoifua and Tungua, Kingdom of Tonga, equidistant from Hunga volcano as submarine samples (∼85 km NE). The glass compositions cover a

10.1029/2024GC011629

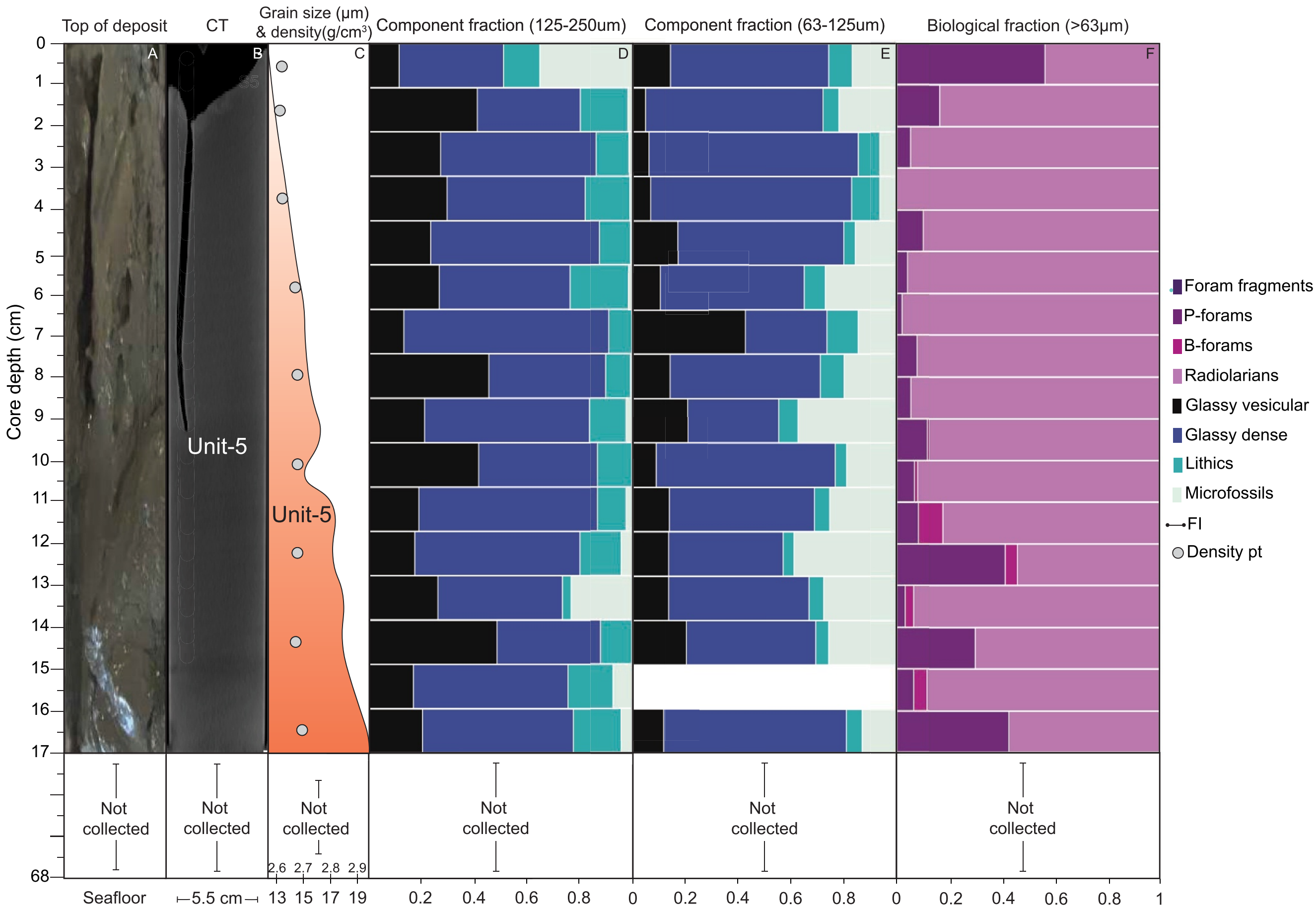

Figure 7. Description of core TC-3. From left to right: (a) true color imagery, (b) CT scan, (c) median grain size (shown as curve) and bulk deposit density (shown as points), (d) componentry of coarser particles (125–250 μm), (e) componentry of particles (63–125 μm), and (f) biological componentry of all particles >63 μm.

broad range of silica contents and vary between grains and between samples (Figure 8). Altogether, compositions range from basaltic-andesite (52.2 wt.% SiO_2) to dacitic (65.6 wt.% SiO_2), with most grains falling within a narrow band around 58 ± 2 wt.% SiO_2 (basaltic andesite/andesite). The chemical composition of the glass in some grains from the scoop samples also falls within that same andesitic area covered by the Hunga volcano (56.8–61.0 wt.% SiO_2). The other grains collected in the scoop samples form two groups with either much lower (52.2–54.7 wt.%) or much higher (65.0–65.6 wt.%) SiO_2 content than the Hunga volcano fresh ash from the 15 January 2022 eruption.

4. Discussion

In the following sections, we first demonstrate that the ash analyzed in the push cores originates from the 15 January 2022 eruption of Hunga volcano (Section 4.1). We then discuss the possible transport mechanisms that led to the deposition of this ash more than 100 km from its source (Section 4.2). Finally, we provide new insights into the transport dynamics using the types of bioclasts found in the two cores (Section 4.3).

4.1. Deposit Source

To ascertain the origin of the ash sampled at the Lau Basin vent sites, we compare their glass geochemical composition to a compilation of glass chemistry of lava from the Lau Basin (Gale et al., 2013; Bézos et al., 2009), the Fonualei Rift and Spreading Center (Escrig et al., 2012), submarine volcanoes of the Tofua arc (Cooper et al., 2022), a breadcrust bomb from the 2014–2015 eruption of Hunga volcano (Colombier et al., 2018), published data on subaerial and submarine ash from the 15 January 2022, eruption of Hunga volcano (Seabrook et al., 2023), and our own data on ash collected on four Tongan islands a day after the eruption (see Figure 8 for

10.1029/2024GC011629

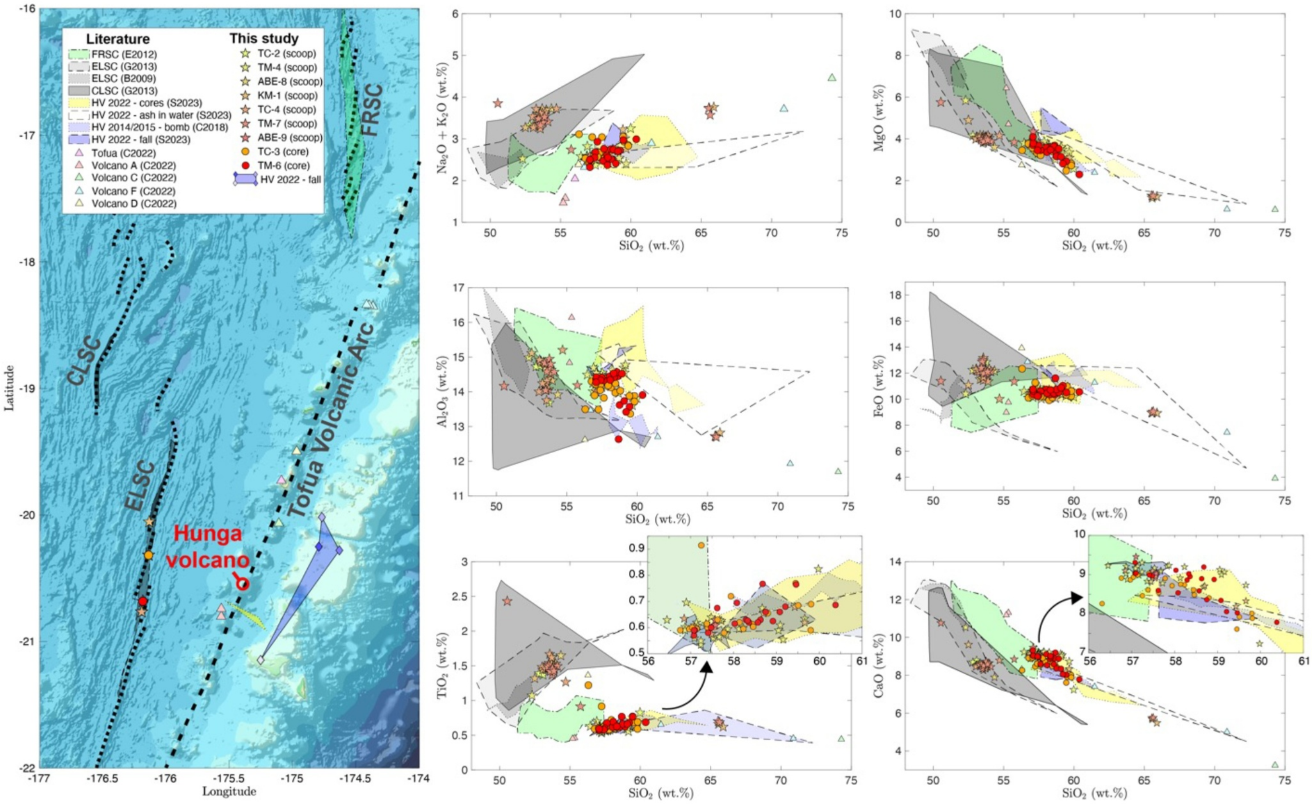

Figure 8. Major element glass compositions of scoop (star) and core (disc) submarine samples analyzed in this study compared to glass compositions of local and regional volcanic rocks collected from the literature. Data from the literature are from: the Fonualei Rift and Spreading Center (FRSC; Escrig et al., 2012; E2012), submarine volcanoes from the Tofua volcanic arc (Cooper et al., 2022; C2022), the Eastern Lau Spreading Center (Gale et al., 2013, and references therein, G2013; Bézos et al., 2009, B2009), the Central Lau Spreading Center (Gale et al., 2013, and references therein), a breadcrust bomb from the 2014–2015 eruption of Hunga volcano (Colombier et al., 2018); subaerial ash fall from the January 2022 eruption of Hunga volcano (Seabrook et al., 2023, S2023; this study, diamond), ash in water (Seabrook et al., 2023), and submarine cores of pyroclastic flow deposits from the January 2022 eruption of Hunga volcano (Seabrook et al., 2023). To facilitate the reading of the graphs, colored zones, rather than individual symbols, are used for most of the data from the literature and the subaerial ash analyzed in this study. Note that the same set of data is presented using individual symbols in the supplementary material. Insets are zoomed-in views of the location of the core samples analyzed in this study. All new and literature data used are available in supplementary material. The Gebco_s2024 grid was used to create the bathymetric map on the left (GEBCO Compilation Group, 2024).

locations of these samples). Data obtained on grains from cores TC-3 (57.1–60.4 wt.% SiO_2) and TM-6 (56.3–59.8 wt.% SiO_2) fall within the same area as those obtained on ash from the 15 January 2022 eruption of Hunga volcano collected on land (Figure 8) or by Seabrook et al. (2023) for all major elements. Core data also fall within the same area as the core data from Seabrook et al. (2023) that were attributed to submarine density currents from the 15 January 2022 eruption of Hunga. Our two push cores, which are a better reflection of the composition of the analyzed deposit than the scoop samples because they sampled only the recently deposited ash, thus come from the 15 January 2022 eruption of Hunga volcano.

More than half of the grains analyzed in the scoop samples have a Hunga's origin. Scoop samples also contain ~40% of grains with a composition like that of lavas from the Lau Basin, and four particles with a composition like that of some grains found in cores of the 15 January 2022, submarine density currents from Hunga volcano (Seabrook et al., 2023; SiO_2 of ~65.5 wt.%). The presence of Lau Basin grains in the scooped samples could be due to either (a) inadvertent scrapping of the underlying volcanic rock with the scoop or (b) scouring of the Lau Basin seafloor via submarine density currents. This could also be explained by the production and dispersal of volcaniclastic material from Lau Basin eruptions. However, that material would be restricted to the lower parts of the deposits as there are no known eruptions in the 4 months between the January 15 Hunga eruption and scoop sampling. Based on the preponderance of Hunga compositions within the scoop deposits, the lack of volcanic material from the Lau Basin in the push cores, and the overwhelming dominance of juvenile material (geological and biological), we are confident that all the observed volcaniclastic deposits that buried the Lau Basin vent sites originated from the 2022 eruption of Hunga volcano.

4.2. Transport Mechanisms: Fall or Flow?

Two main transport mechanisms can be envisioned to explain the presence of 15 January 2022 Hunga deposits located 80–100 km west from their source: (a) ash fall from an atmospheric plume that then settled through the up to ~2.8 km of seawater before deposition on the ocean floor; and/or (b) seafloor hugging submarine density current(s) that traveled SW and NW from the volcano down to the Lau Basin.

4.2.1. TM-6 Units-1, 2, and 3: SW Submarine Density Current From Hunga Volcano

For the reasons detailed below, we interpret Units-1-3 in TM-6 to be produced by submarine density currents. Due to the fine-grained nature and structural features observed in these basal layers of TM-6, this deposit is interpreted in light of the standard sequence of structures in an "ideal" fine-grained turbidite unit (Figure S14 in Supporting Information S1; Bouma, 1962; Stow & Shanmugam, 1980). In this sequence, the deposit is divided into nine subdivisions labeled T_0-T_8 based on their sedimentological characteristics and structure. Since juvenile ash is the dominant grain type throughout our push cores, we categorize sediment lithology based on the entrained material (lithics and bioclasts), following the classifications of (Stow & Shanmugam, 1980).

Discontinuous lenticular laminae in the basal Unit-1 are common in thin turbidite facies (Bouma et al., 1986; Stow & Smillie, 2020). They are consistent with bed-surface particle sorting sourced from fluid turbulence in a viscous sublayer of a fine-grained density current (Al-Mufti & Arnott, 2024; D. A. V. Stow & Bowen, 1978; D. A. V. Stow & Shanmugam, 1980; D. Stow & Smillie, 2020). Unit-1 contains a subtle reverse grading, which is commonly attributed to kinetic sieving in coarse granular flows (Figure S15 in Supporting Information S1) (Legros, 2002). In our much finer deposit, we rather envision two mechanisms that could explain this basal reverse grading: (a) the rapid deposition of a turbidity current during which fines are no longer effectively trapped as the rate of suspension-load fallout decreases (Sylvester & Lowe, 2004) and/or (b) a waxing-depletive current producing rapid suspension fallout followed by basal traction (Kneller & Branney, 1995). Unlike basal reverse grading found in both proximal and distal deposits of submarine currents at Montserrat (Stevenson et al., 2013; Trofimovs et al., 2008), proximal submarine current deposits at Hunga do not exhibit such features (Clare et al., 2023). Thus, we do not favor source flux fluctuations as the cause of the observed reverse grading within Unit-1 but rather attribute this reverse grading to the first mechanism proposed. Therefore, we interpret Unit-1 is equivalent to layer T_0 of the ideal fine-grained turbidite unit (Figure S14 in Supporting Information S1). Entrained grains within Unit-1 are primarily silt-clay grains with an averaged 12% carbonate content and sporadic sand-sized foraminifera that we correlate to carbonate mud. Immense erosional scours <10 km of Hunga's volcanic flanks account for 3.5 km^3 of eroded sediment by submarine density currents (Clare et al., 2023; Seabrook et al., 2023). The hemipelagic lithology (carbonate mud), even at this distance from the source, is consistent with evidence of a high volume of erosion and entrainment in proximal regions.

Subtle climbing ripples in Unit-2 are a product of silt-loading into small-scale layers like bedforms sand-grains form found in coarser turbidity currents (Figure S15 in Supporting Information S1) (McBride et al., 1975). Unit-2 lithology is consistent with Unit-1 with an abrupt absence of carbonate content. We attribute this to size/density sorting of the sand-sized foraminifera in Unit-1 during suspension fallout of a density current. Unit-2 is thus like sub-divisions T_1-T_2 of a fine-grained turbidite unit (Figure S14 in Supporting Information S1).

Distinction between deep-sea facies, turbidites and hemipelagites is often ambiguous. There can be overlap of deposit mechanics, characteristics, and geographic location between facies, making distinction based on sedimentary characteristics alone difficult (Stow & Smillie, 2020). Coloration and structure of these basal units strongly resemble hemipelagite collected beneath Hunga 2022 deposits in Clare et al. (2023). Micro-fabric textures in Units 1–2 are discontinuous and coarse grains (dark spheres) appear randomly distributed (Figure S15 in Supporting Information S1). The upper boundary between Unit-2 and Unit-3 is sharp and continuous, marked by an abundance of coarse foraminifera. These features may be consistent with a hemipelagite produced by a density current prior to the eruption. However, the continuous grading throughout TM6 (Figure S4 in Supporting Information S1), the absence of sediment at this site as of 2019 (Beinart et al., 2024) and the abundance of juvenile ash with a Hunga 2022 composition within Units 1–2 (Figures S9 and S10 in Supporting

10.1029/2024GC011629

Information S1) support our initial interpretation; Units 1–2 represent the base of a fine-grained density current produced by the 2022 Hunga volcano eruption.

Regular parallel laminae, as seen in Unit-3, are common in decelerating dilute flows (Figure S15 in Supporting Information S1) (Kranck, 1984; Piper, 1978; Stow & Shanmugam, 1980; Talling et al., 2012), corresponding to sub-division T_3 in Figure S14 in Supporting Information S1. They are a depositional product of increased shear at the basal boundary (Unit-2) leading to size/density differential settling between sand/silt-sized foraminifera and clay (Stow & Bowen, 1978). A conservative settling estimate of the entire 4-cm laminae in Unit-3 is 4–6 days based on Equation 4 of Stow and Bowen (1978). The fine-grained lithology of Unit-3 entrained volume and abundance of foraminifera is categorized as a carbonate mud.

4.2.2. TM-6 Unit-4: Ash Fall and Settling Through the Water Column

The structureless and subtly graded Unit-4 in TM-6 could be attributed to structural divisions T_6 or T_7 of the turbidite sequence (Figures S14 and S15 in Supporting Information S1), but the abrupt changes in almost all characteristics suggest otherwise. Unit-4 is distinct from the underlying Unit-3 in terms of color, structure, and sedimentological characteristics (size, density, bioclasts composition). Most notably, there is a near absence of bioclasts >63 μm and a pale coloration of the clay-sized lithic fraction. These changes point to a shift in the type of deposition, to a much less dynamic mode of transport compared to Units-1-3, unable to erode carbonate sediments and fragment forams, although it is also possible that earlier density currents (Units-1–3) have shielded seafloor sediments from erosion. We interpret Unit-4 has another origin.

TM-6, like all vent fields sampled in this study, is located well within the ~400 km radius of the umbrella cloud produced during the 15 January 2022 eruption of Hunga volcano (Van Eaton et al., 2023). The grain sizes measured in Unit-4 (~15 μm in median diameter, with >60% of the mass made of grains <32 μm) are consistent with the grain size estimated for the plume (<100 μm, Kelly et al., 2024). Using the isopach map from Kelly et al. (2024), we estimate ash fall thickness directly over TM-6 to be around 2 cm, consistent with the 1–2 cm thickness of Unit-4.

Clare et al. (2023) estimated the proximal velocity of the 15 January 2022 Hunga submarine density currents to be 32–122 km/hr, based on the timing of damage to domestic and international submarine cables located several tens of kilometers away from the volcano. Even if the flow velocities largely declined before the flows reached the Lau Basin, the submarine density currents would have reached locations TC-3 and TM-6 less than a few hours after the start of the eruption, at least for their basal parts. Ignoring possible production of vertical density currents (Manville & Wilson, 2004), we estimate an order of magnitude for the time it took median particles found in Unit-4 to fall from (a) the lower part of the plume (~10–20 km in altitude; Gupta et al., 2022) to the surface of the ocean, and (b) from the sea surface down to the bottom of the ocean (~2.32 km below the ocean surface at TM-6). We use the settling velocity, w_s (m/s) expressed as

$$w_s = \left(\Delta\rho_s\, g\, d^2\right) / (18\mu), \tag{1}$$

where d (m) is the particle diameter, $\Delta\rho_s = \rho_s - \rho$ (kg/m^3) is the particle minus fluid density (negligible for air and taken at 1050 kg.m^{-3} for seawater), g (9.81 m.s^{-2}) is the acceleration of gravity, and μ is the dynamic viscosity of the fluid (~1.8×10^{-5} Pa.s for air, 1.5×10^{-3} Pa.s for water at 2°C). Assuming a particle 15 μm in diameter (median particle diameter in Unit-4) with a density of 2,800 kg.m^{-3} gives a settling velocity of about 19 mm/s in air and 0.14 mm/s in water, and thus a travel time of 6–12 days from the plume to the surface of the ocean, and another 6 months to settle to the bottom of the ocean. These times are order of magnitude maximum estimates because it is more than likely that these small particles fell as aggregates in the atmosphere and were caught in suspension by lateral currents and density interfaces (Bradley, 1965; Taddeucci et al., 2011). If rapid fallout of ash from the mixed layer occurred, vertical density current velocities would overcome individual Stokesian particle settling velocities calculated here (Manville & Wilson, 2004). Assuming (a) the size of these aggregates is like that reported by Taddeucci et al. (2011) for the ash ejected during 2010 eruption of Eyjafjallajökull (~1 mm), and (b) making the conservative hypothesis that these aggregates remained intact until their impact on the ocean floor, it would still require a total travel time of more than a day for these aggregates to fall from the plume to the bottom of the ocean floor (in the absence of settling acceleration). This is consistent with the settled particles forming the uppermost Unit-4, located above the density current deposit (Units-1–3).

Our interpretation of Units-1-4 in core TM-6 is similar to cores presented in Clare et al. (2023), who report density current-related ash-sized deposits that are 34 cm thick at ~23 km SE of our core TM-6 (core 36-22 in Figure S1 in Supporting Information S1 of Clare et al., 2023), 23 cm thick at ~20 km to the SSE (core 90-23), 45 cm thick at ~36 km to the SSW (core 96-31), and 4.5 cm thick at ~36 km to the SW (core 95-24). These cores exhibit the same overall characteristics such as coloration, structure, and grain size sorting as TM-6, with a density current deposit structure that we correlate to our Units-1-3 and whose total thickness varies from 4.5 cm (core 95-24) to 45 cm (core 96-31). Using the photographs and logs of the cores presented in the supplementary material of Clare et al. (2023), Units-1–2 in these cores are ~14 cm thick in core 36-22 and core 90-23, and 10 cm thick in core 96-31. Units-1-2 do not appear in core 95-24. The more dilute Unit-3 is 35 cm in core 96-31, 20 cm in core 36-22, 9 cm in core 90-23, and 4.5 cm in core 95-24. Transition from Unit-2 to Unit-3 is quite sharp in core 36-22 (like in TM-6), whereas it is more progressive in core 90-23. We thus interpret that deposits at Southern sites Tahi Moana (core TM-6) and Abe (scoop ABE-9) are distal lithological facies of Hunga density current(s) directed SW, following the pathway of TAN2206 proximal cores 31-20, 87-21, 83-04, 36-22, 90-23, 96-31 and 95-24 (Clare et al., 2023). Erosion and depositon are well documented along this SW path (Clare et al., 2023; Seabrook et al., 2023), with >120 m erosional scours and 40 m depositional lobes located along Hunga's flanks.

Similarly, in the four cores from Clare et al. (2023), the density current deposit is overlaid by what is interpreted as a 1.5–7.5-cm-thick ash fall deposit that we interpret to be the same as our Unit-4.

4.2.3. Unit-5: Northwestward Submarine Density Current From Hunga Volcano

Core TC-3 is 16 cm long but only samples the upper ~25% of a deposit that is 68 cm. Thicknesses measured a few tens of meters away from TC-3 vary by up to 15 cm (53–68 cm, see Table 1), about five times the estimated uncertainty associated with thickness measurement. Fall deposits tend to blanket pre-existing topography. Although an uneven distribution of ash-fall deposits due to weak laterally advecting bottom currents cannot be precluded, the measured deposit thickness at TC-3 (53–68 cm) is not consistent with the predicted ash fall from the eruptive plume (Kelly et al., 2024). Strong normal grading, concentrated bioclasts, and deposit thickness of Unit-5 are more consistent with sub-division T_6 (graded mud) of the Stow sequence (Figure S14 in Supporting Information S1), which is formed by gradual suspension fallout of a dilute density current (Stow & Shanmugam, 1980). Fine-grained turbidite deposits often do not show a full sequence of structures (Stow & Shanmugam, 1980). Lower sequences (T_0-T_4), as seen in TM-6, are found more commonly near channels and fan lobes, while upper sequences (T_4-T_8) are more common off axis and in outer fans in the abyssal plain (Stow & Shanmugam, 1980). Given that coring at TC-3 fails to penetrate and collect the entire Hunga deposit, we cannot exclude the presence of basal sequences (T_0-T_4) at TC-3 below what was cored. We thus interpret that the deposits at the northern sites Tow Cam (core TC-3) and Kilo Moana (scoop KM-1) were sourced from density current(s) directed NW from Hunga volcano, following the pathway of TAN2206 proximal core 65-30 (Clare et al., 2023).

4.3. Dynamics of the Submarine Density Currents

Identifying the source of entrainment of the submarine density currents can aid in tracing the dynamics of their ~100 km runout from the Hunga volcano to the Lau Basin (Figure 9). In this last section, we do so using the bioclastic content, which has commonly been used to identify density current head sources at the base of slopes (Hayward et al., 2022; Talling et al., 2007; Usami et al., 2017).

4.3.1. SW Submarine Current (Core TM-6)

Poor preservation of foraminifera within the basal layer of TM-6 represents carbonate dissolution at the sediment/water interface (Sulpis et al., 2017). The rate of carbonate dissolution increases with depth in the ocean. Rapid increase in dissolution occurs at two depth-interfaces, the calcium saturation depth (CSD) and calcium carbonate depth (CCD). Above the CSD, carbonate microfossils experience little to no dissolution. At depths between the CSD and CCD (lysocline), carbonate microfossils begin to rapidly breakdown at the sediment/water interface, producing poorly preserved foraminifera and red clay. The massive erosional scours observed along Hunga's flanks (Clare et al., 2023; Seabrook et al., 2023) sit >500 m above the modern CSD, located around 3,000 m (Sulpis et al., 2018). For this reason, entrained foraminifera and red clay within the basal layer must have an alternate source than proximal sediments. Another possible source of basal entrainment is much further away from Hunga volcano, near the Eastern Lau Spreading Center (ELSC). Daesslé and Cronan (2001) collected older

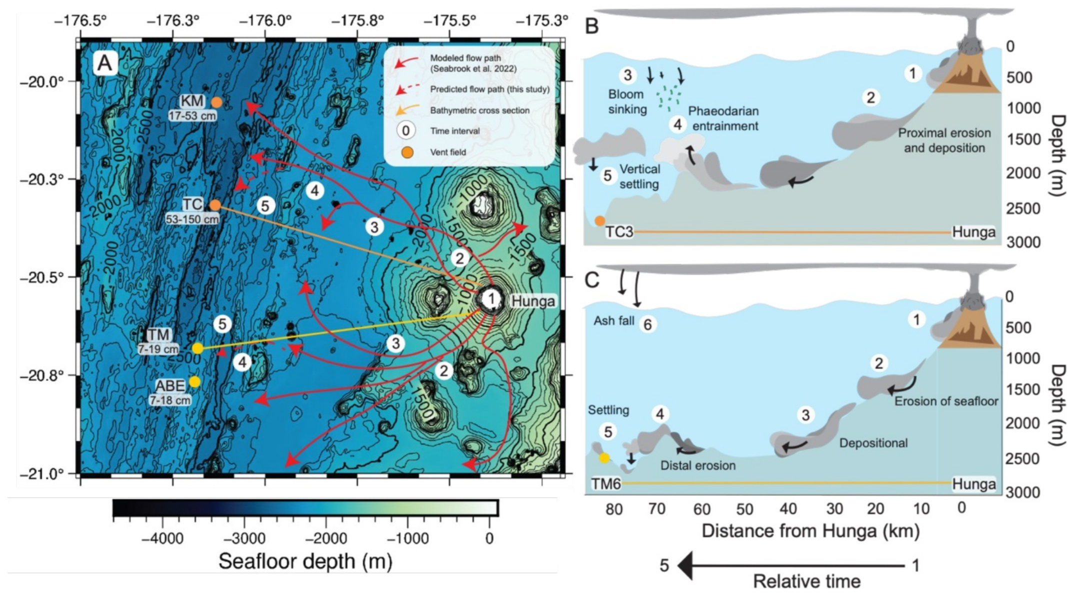

Figure 9. Bathymetry sourced from Taylor et al. (1996). (a) Shaded contour plot showing bathymetric cross sections, modeled flow paths from Seabrook et al. (2023) and predicted paths toward TC-3 and TM-6 (this study). Range of deposit thickness at each vent field shown in cm. (b) Illustration of the flow path for TC3 and its corresponding bathymetric cross sections as drawn in part (a). Significant time markers numbered along path. 1- Focusing of flows between former island Hunga-Tonga and Hunga-Ha'apai. 2- Proximal erosional scours and depositional lobes as outlined in Clare et al. (2023). 3- Sinking of phytoplankton surface bloom. 4- Density current entrainment of phaeodarians within the water column. 5- Vertical settling of dilute density current. (c) Predicted flow path for TM6 with bathymetric cross section. 1-remains consistent as in (b. 2- Erosional granular density currents ∼122 km/hr (Clare et al., 2023). 3- Depositional density current ∼30 km/hr (Clare et al., 2023). 4- Distal erosion of older volcaniclastic deposits from Daesslé and Cronan (2001). 5- Vertical settling of dilute current. 6- Atmospheric ash fall settling.

volcaniclastic sediments off axis of the ELSC. These are reddish-brown deposits rich in volcanic ash and encrusted carbonates, similar to the basal layer of TM-6. The volcanogenic component has a Tofua arc signature (Riech et al., 1990), linking a history of volcaniclastic density currents from Tofua arc volcanoes. Similar findings from Cronan et al. (1984) point to Fe-oxide, carbonate rich sediments (20%–40%) within the Eastern basin (Cronan et al., 1984; Moorby, 1986). Lower effective density and smaller grain-size of bioclasts can affect their transport potential, resulting in distal deposition; however, proximal cores in Clare et al. (2023) do not exhibit any reddish/brown coloration or bioclasts. We conclude that the SW density current reached a secondary erosional threshold near the Western margin of the ELSC (80 km from their source), which was not previously observed (Figure 9).

4.3.2. NW Submarine Current (Core TC-3)

Depositional lobes 12-km wide and 40-m thick were observed within 25 km NW of the edifice (Figures 2a and Clare et al., 2023). Whether alternate deposition and erosional regimes occurred along the NW path down to the ELSC is uncertain because of the absence of observations. Since our coring sampled only the upper part of the entire Hunga 2022 deposit at TC-3, we cannot rule out overall structural similarities between the deposits of the NW and SW currents. We can, however, distinguish the NW and SW currents' deposits based on their divergent bioclastic compositions. The main observations used to suggest that there were at least two different lithological sources for TC-3 and TM-6 deposits are (a) the ubiquity of siliceous bioclasts (radiolarians and diatoms) in TC-3 (12%) while they are quasi absent in TM-6 (<1%), whereas 2) the abundance of calcareous foraminifera (7%–8%) found in TM-6 while they are limited throughout TC-3 (∼3%). The high radiolaria:foraminifera ratio observed in TC-3 can be explained by (1) differences in transport potential, (2) sampling of abnormally high radiolarian: foraminifera concentrations, or (3) entrainment of additional radiolaria from within the water column:

(1) Siliceous bioclasts found within TC-3 are smaller and lighter than calcareous bioclasts found in TM-6 (Takahashi & Be, 1984; Takahashi & Honjo, 1983). A clear separation of bioclastic content between the

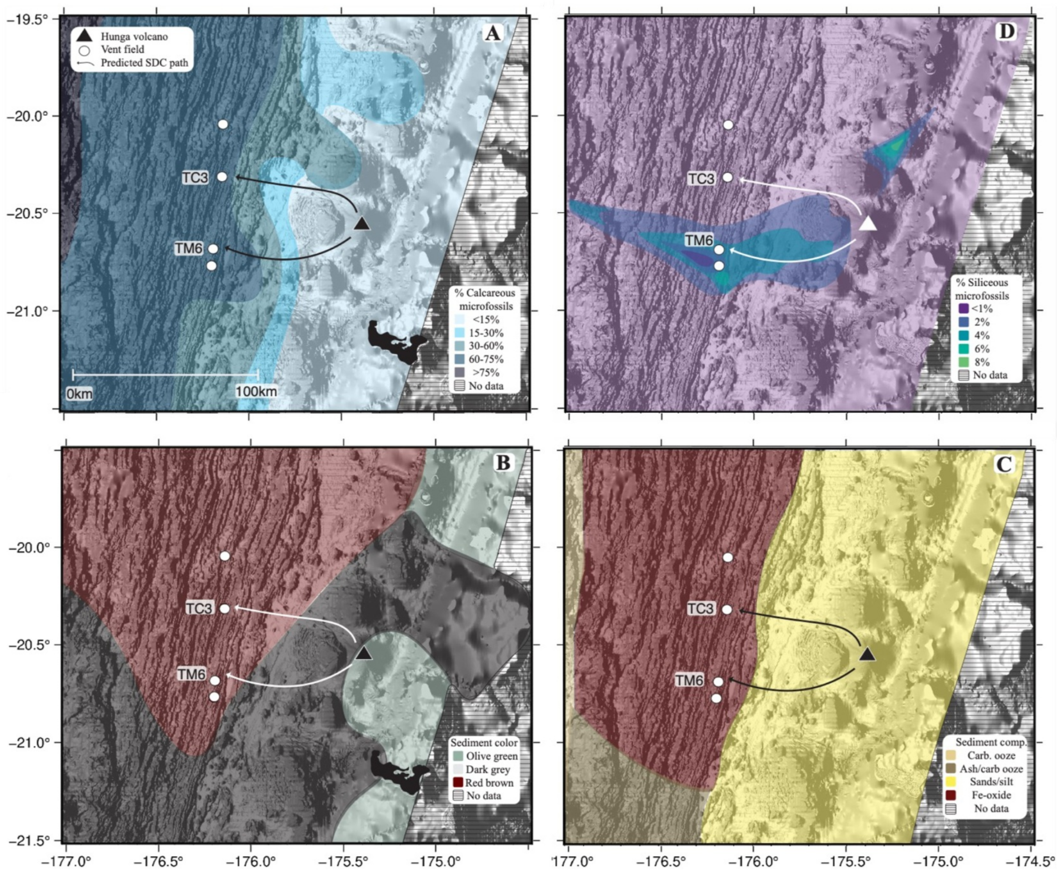

Figure 10. Regional deposit and bioclastic analysis collected from Moorby (1986), Daesslé and Cronan (2001) and Clare et al. (2023). (a) Observed volcaniclastic deposits from past density currents (Daesslé & Cronan, 2001), and Hunga sourced density currents (this study and Clare et al., 2023). (b) Siliceous bioclastic abundance (%). (c) Calcareous bioclastic abundance (%). (d) Primary sediment composition of smear slides.

two sites may suggest density sorting during the emplacement of the submarine density current; as currents progressed from Hunga, coarse/dense foraminifera are likely to have been deposited first, followed by radiolarians. Assuming a balanced foraminifera:radiolarian entrainment, the silicate dominant TC-3 may represent a later state of the NW current in which forams have settled out more proximally (note that the same runout stage estimation cannot be made within TM-6 due to a lack of bioclast diversity).

(2) Previous mapping of the Lau Basin showed that siliceous bioclasts exist in distinct patches (Moorby, 1986), with the only known source of concentrated radiolarians being siliceous ooze clusters 20 km NNW and 80 km SW of Hunga (Moorby, 1986; Figure 10). The high radiolaria:foraminifera ratio observed in TC-3 is not consistent with the calcareous dominant sediments that constitute the Tofua Arc and Lau Basin (Figure 10), but the absence of sediment samples directly NW of Hunga makes it difficult to confirm the pre-eruptive southern extent of siliceous ooze. It is possible that highly concentrated siliceous oozes mapped North of 18°S extend farther south than previously observed (Moorby, 1986) and were sampled by the NW submarine current.

(3) Although not quantitatively analyzed, a large proportion of the siliceous bioclasts within TC-3 are modern phaeodarians. Phaeodarians, in contrast to polycistina radiolaria, dissolve rapidly in the water column and are rarely preserved in large quantities within sediments (Biard et al., 2018; Takahashi & Honjo, 1983). The anomalously high preservation rates of modern phaeodarians in TC-3 allude to their recent and rapid entrainment from the water column. The density current may have entrained additional radiolaria from within the water column, which could be a product of the eruption-induced phytoplankton bloom (Barone et al., 2022; Yoon et al., 2023) related to fall deposits in this region (Kelly et al., 2024; Mastin et al., 2024; Van Eaton et al., 2023). Given the absence of a clear layer of ash fall in TC-3 (unlike in TM-6 with Unit-4), it is

unlikely that phaeodarians found in TC-3 were entrained by vertical settling of ash fall. However, a thick, highly diluted density current could entrain sinking phaeodarians located low in the water column rapidly enough to preserve their delicate skeletons, explaining the abnormally high radiolaria:foraminifera ratio observed in TC-3.

5. Conclusions

This paper characterizes deep submarine volcaniclastic deposits from the Lau Basin collected via cores and scoops. Sampling occurred about 80–100 km west of Hunga volcano, Kingdom of Tonga volcano, within four months after its 15 January 2022 eruption. Sampled cores are fine-grained and rich in juvenile volcanic material and bioclasts. We show that the deposit has the same major element composition as ash from the 15 January 2022 eruption of Hunga volcano collected on land immediately after the eruption and also similar to submarine cores collected between Hunga volcano and our sample location by Seabrook et al. (2023). We thus conclude that the collected deposits are from the 15 January 2022 eruption of Hunga, providing a rare opportunity to study fresh, distal, undisturbed deposits from a submarine explosive eruption.

Using core structure, grainsize, componentry, composition, and density, we demonstrate that these deposits were primarily emplaced by submarine density currents. We show that they correspond to the distal portions of at least two large submarine density currents flowing roughly SW and NW from the volcano, as previously reported by Seabrook et al. (2023) and Clare et al. (2023). Our data help understand the syn-eruptive volcaniclastic transport from a shallow submarine volcano to the deep-sea. We use the abundance of bioclasts of different types to demonstrate the erosional evolution of the density currents and provide insight into source pathways, building on previous submarine density current studies. Comparison of bioclast and lithic composition with background deposits of the Lau Basin uncovered a secondary erosional regime >80 km from the source, which was not previously documented for these currents. Density current pathways identified by bioclast tracers also suggest that separate flows were triggered to the NW and SW of Hunga, producing distinct deposits in the North and South extents of the central basin. The integrated use of micropaleontological, sedimentological and geochemical tools unveiled a unique view under the ocean's surface of the Hunga eruption.

Submarine density currents can transport voluminous sediment for up to hundreds to thousands of kilometers across limited topographic gradients. In many parts of the world, submarine particulate flows are the dominant sediment flux source in the deep ocean. In the Lau Basin, volcanic-induced flows are the dominant sediment, carbon, and nutrient influx. The 2022 eruption of Hunga volcano provides a rare opportunity to study deep sea volcaniclastic deposits of a known source. Sampling of the distal submarine density currents unveils strong erosive behavior, ultimately remobilizing bioclastic-concentrated sediments to the Lau Basin, more than 80 km from the source. Opportune erosion and entrainment by volcanic-induced submarine density currents may play a greater role in carbon, and nutrient transport into deep sea basins than previously thought. Direct observation of a modern mass-sedimentation event with a known source is a rare contribution to the marine sedimentological record, as estimations of sediment influx into the deep-sea are widely underreported. With an observed latitudinal extent of 220 km, a longitudinal extent of 100 km, deposits up to 150 cm in the far field of the basin, and the ability to overrun positive slopes, such events may have runout distances well beyond what has been observed and likely alter the affected benthos ecosystem. Ongoing voyage campaigns tied to this work are thus vital to understand not only the extent of the 15 January 2022 Hunga sedimentation event but also the effect of rapid sedimentation in the fragile deep sea.

Acknowledgments
We thank the Kingdom of Tonga and the ministry of Lands and Natural Resources for permission to work in their waters. We thank the entire TN401 scientific party and crew of the R/V Thomas G. Thompson and ROV *Jason* II for their roles in sampling and observations. NSF REU student I. Yueh (WWU) assisted with video analyses of ash thickness data. Any use of trade, firm, or product names is for descriptive purposes only and does not imply endorsement by the U.S. Government. We thank Kurt Langworthy for his assistance and training on analyzing samples under SEM at CAMCOR Nanofabrication and Imaging Facility. We thank P. Walzack, D. Clague, and D. Fornari for their aid in developing a core retrieval system while onboard. We thank M. Cheseby at the Oregon State University Marine and Geology Repository for her assistance in scanning and storing the cores. We thank J. Dufek, N. Llopis Monferrer, M. Cevel, K. McKee, V. Sahakian, M. Cascante Matamoros, J. Donnenfield, E. Fraile Nuez, B. Barone, J. Scheffler and D. Tran for discussions and feedback related to this study. The authors declare no financial conflicts of interest for any author or competing interests with respect to the results of the paper. This work was supported by NSF awards OCE-1736932 (R.A.B.), OCE-1737382 (S.M.A.), OCE-1737145 (C.M.Y.), and EAR-2240044 (T.G.). KEF and LJK were supported by NASA Grant 80NSSC20K1450 and KEF acknowledges the University of Oregon Meierjurgen Visiting Faculty Fellowship for enabling collaboration. MAC and IAY were supported by Natural Environment Research Council Grant sNE/X00239X/1 and NE/X003272/1. RJC and MJ were supported by the Australian Research Council Discovery Project DP230100026. AVE was supported by the USGS and Volcano Hazards Program. SJC and JPM were supported by NZ Ministry of Business, Innovation amd Employment Endeavor Research Programmes UOAX1913 and UOA24103.

Data Availability Statement

All sedimentological and micropaleontological data presented in this study may be accessed through the following open access data repository (Chaknova, 2024). Geochemical data are available within the supplementary information (Table S3–S5 in Supporting Information S1).

References

Al-Mufti, O. N., & Arnott, R. W. C. (2024). The origin of planar lamination in fine-grained sediment deposited by subaqueous sediment gravity flows. *The Depositional Record*, *10*(5), 496–514. https://doi.org/10.1002/dep2.257

Aze, T., Ezard, T. H. G., Purvis, A., Coxall, H. K., Stewart, D. R. M., Wade, B. S., & Pearson, P. N. (2011). A phylogeny of Cenozoic macroperforate planktonic foraminifera from fossil data. *Biological Reviews*, *86*(4), 900–927. https://doi.org/10.1111/j.1469-185X.2011.00178.x

Baker, E. T., Massoth, G. J., de Ronde, C. E. J., Lupton, J. E., & McInnes, B. I. A. (2002). Observations and sampling of an ongoing subsurface eruption of Kavachi volcano, Solomon Islands, May 2000. *Geology*, *30*(11), 975–978. https://doi.org/10.1130/0091-7613(2002)030<0975:OASOAO>2.0.CO;2

Barone, B., Letelier, R. M., Rubin, K. H., & Karl, D. M. (2022). Satellite detection of a massive phytoplankton bloom following the 2022 submarine eruption of the Hunga Tonga-Hunga Haʻapai volcano. *Geophysical Research Letters*, *49*(17), e2022GL099293. https://doi.org/10.1029/2022GL099293

Baumberger, T., Lilley, M. D., Resing, J. A., Lupton, J. E., Baker, E. T., Butterfield, D. A., et al. (2014). Understanding a submarine eruption through time series hydrothermal plume sampling of dissolved and particulate constituents: West Mata, 2008–2012. *Geochemistry, Geophysics, Geosystems*, *15*(12), 4631–4650. https://doi.org/10.1002/2014GC005460

Beinart, R. A., Arellano, S. M., Chaknova, M., Meagher, J., Davies, A. J., Lopresti, J., et al. (2024). Deep seafloor hydrothermal vent communities buried by volcanic ash from the 2022 Hunga eruption. *Communications Earth & Environment*, *5*(1), 1–10. https://doi.org/10.1038/s43247-024-01411-w

Bézos, A., Escrig, S., Langmuir, C. H., Michael, P. J., & Asimow, P. D. (2009). Origins of chemical diversity of back-arc basin basalts: A segment-scale study of the Eastern Lau Spreading Center. *Journal of Geophysical Research*, *114*(B6). https://doi.org/10.1029/2008JB005924

Biard, T., Krause, J. W., Stukel, M. R., & Ohman, M. D. (2018). The significance of giant Phaeodarians (Rhizaria) to biogenic silica Export in the California Current Ecosystem. *Global Biogeochemical Cycles*, *32*(6), 987–1004. https://doi.org/10.1029/2018GB005877

Bouma, A. H. (with Internet Archive). (1962). *Sedimentology of some flysch deposits: A graphic approach to facies interpretation*. University Microfilms International. Retrieved from http://archive.org/details/sedimentologyofs0000boum

Bouma, A. H., Coleman, J. M., & Meyer, A. W. (1986). *Initial reports of the Deep Sea Drilling Project, 96* (Vol. 96). U.S. Government Printing Office. https://doi.org/10.2973/dsdp.proc.96.1986

Bradley, W. H. (1965). Vertical density currents. *Science*, *150*(3702), 1423–1428. https://doi.org/10.1126/science.150.3702.1423

Burnett, D. R., & Carter, L. (2017). International submarine cables and biodiversity of areas beyond national jurisdiction: The cloud beneath the sea. *Brill Research Perspectives in the Law of the Sea*, *1*(2), 1–72. https://doi.org/10.1163/24519359-12340002

Carey, R. J., Wysoczanski, R., Wunderman, R., & Jutzeler, M. (2014). Discovery of the largest historic silicic submarine eruption. *Eos, Transactions American Geophysical Union*, *95*(19), 157–159. https://doi.org/10.1002/2014EO190001

Carey, S. N., & Schneider, J.-L. (2011). Chapter 7—Volcaniclastic processes and deposits in the deep-sea. In H. HüNeke & T. Mulder (Eds.), *Developments in Sedimentology* (Vol. 63, pp. 457–515). Elsevier. https://doi.org/10.1016/B978-0-444-53000-4.00007-X

Carter, L., Gavey, R., Talling, P. J., & Liu, J. T. (2015). Insights into submarine Geohazards from breaks in Subsea telecommunication cables. *Oceanography*, *27*(2), 58–67. https://doi.org/10.5670/oceanog.2014.40

Cassidy, M., Watt, S. F. L., Palmer, M. R., Trofimovs, J., Symons, W., Maclachlan, S. E., & Stinton, A. J. (2014). Construction of volcanic records from marine sediment cores: A review and case study (Montserrat, West Indies). *Earth-Science Reviews*, *138*, 137–155. https://doi.org/10.1016/j.earscirev.2014.08.008

Chadwick, W. W., Jr., Cashman, K. V., Embley, R. W., Matsumoto, H., Dziak, R. P., de Ronde, C. E. J., et al. (2008). Direct video and hydrophone observations of submarine explosive eruptions at NW Rota-1 volcano, Mariana arc. *Journal of Geophysical Research*, *113*(B8). https://doi.org/10.1029/2007JB005215

Chaknova, M. (2024). TN401 Lau Basin samples from eruption of Hunga volcano 2022 [Dataset]. *Zenodo*. https://doi.org/10.5281/zenodo.14064550

Clare, M. A., Yeo, I. A., Watson, S., Wysoczanski, R., Seabrook, S., Mackay, K., et al. (2023). Fast and destructive density currents created by ocean-entering volcanic eruptions. *Science*, *381*(6662), 1085–1092. https://doi.org/10.1126/science.adi3038

Colombier, M., Scheu, B., Wadsworth, F. B., Cronin, S., Vasseur, J., Dobson, K. J., et al. (2018). Vesiculation and quenching during surtseyan eruptions at Hunga Tonga-Hunga Ha'apai Volcano, Tonga. *Journal of Geophysical Research: Solid Earth*, *123*(5), 3762–3779. https://doi.org/10.1029/2017JB015357

Cooper, L., Plank, T., Arculus, R., Hauri, E., & Kelley, K. A. (2022). Arc–Backarc Exchange along the Tonga–Lau system: Constraints from volatile elements. *Journal of Petrology*, *63*(8), egac072. https://doi.org/10.1093/petrology/egac072

Crisp, J. A. (1984). Rates of magma emplacement and volcanic output. *Journal of Volcanology and Geothermal Research*, *20*(3), 177–211. https://doi.org/10.1016/0377-0273(84)90039-8

Cronan, D. S., Hodkinson, R., Moorby, S. A., Glasby, G. P., Knedler, K., & Thomson, J. (1984). Hydrothermal and volcaniclastic sedimentation on the Tonga-Kermadec Ridge and in its adjacent marginal basins. *Geological Society, London, Special Publications*, *16*(1), 137–149. https://doi.org/10.1144/GSL.SP.1984.016.01.10

Daesslé, L. W., & Cronan, D. S. (2001). Hydrothermal input in recent sediments proximal to the eastern Lau spreading Centre, Lau Basin, SW Pacific. *Ciencias Marinas*, *27*(4), 635–659. Article 4. https://doi.org/10.7773/cm.v27i4.496

Deardorff, N. D., Cashman, K. V., & Chadwick, W. W. (2011). Observations of eruptive plume dynamics and pyroclastic deposits from submarine explosive eruptions at NW Rota-1, Mariana arc. *Journal of Volcanology and Geothermal Research*, *202*(1), 47–59. https://doi.org/10.1016/j.jvolgeores.2011.01.003

Du Preez, C., & Fisher, C. R. (2018). Long-term stability of Back-Arc Basin hydrothermal vents. *Frontiers in Marine Science*, *5*. https://doi.org/10.3389/fmars.2018.00054

Embley, R. W., Tamura, Y., Merle, S. G., Sato, T., Shizuka, O. I., Chadwick, W. W., Jr., et al. (2014). Eruption of South Sarigan seamount, Northern Mariana Islands: Insights into hazards from submarine volcanic eruptions. *Oceanography*, *27*(2), 24–31. https://doi.org/10.5670/oceanog.2014.37

Engwell, S. L., Sparks, R. S. J., & Carey, S. (2014). Physical characteristics of tephra layers in the deep sea realm: The Campanian Ignimbrite eruption. *Geological Society, London, Special Publications*, *398*(1), 47–64. https://doi.org/10.1144/SP398.7

Ercilla, G., Casas, D., Alonso, B., Casalbore, D., Galindo-Zaldívar, J., García-Gil, S., et al. (2021). Offshore geological hazards: Charting the Course of progress and future Directions. *Oceans*, *2*(2), 393–428. https://doi.org/10.3390/oceans2020023

Escrig, S., Bézos, A., Langmuir, C. H., Michael, P. J., & Arculus, R. (2012). Characterizing the effect of mantle source, subduction input and melting in the Fonualei Spreading Center, Lau Basin: Constraints on the origin of the boninitic signature of the back-arc lavas. *Geochemistry, Geophysics, Geosystems*, *13*(10). https://doi.org/10.1029/2012GC004130

Fauria, K. E., Jutzeler, M., Mittal, T., Gupta, A. K., Kelly, L. J., Rausch, J., et al. (2023). Simultaneous creation of a large vapor plume and pumice raft by the 2021 Fukutoku-Oka-no-Ba shallow submarine eruption. *Earth and Planetary Science Letters*, *609*, 118076. https://doi.org/10.1016/j.epsl.2023.118076

Ferrini, V. L., Tivey, M. K., Carbotte, S. M., Martinez, F., & Roman, C. (2008). Variable morphologic expression of volcanic, tectonic, and hydrothermal processes at six hydrothermal vent fields in the Lau back-arc basin. *Geochemistry, Geophysics, Geosystems*, *9*(7). https://doi.org/10.1029/2008GC002047

Freundt, A., Schindlbeck-Belo, J. C., Kutterolf, S., & Hopkins, J. L. (2023). Tephra layers in the marine environment: A review of properties and emplacement processes. *Geological Society, London, Special Publications*, *520*(1), 595–637. https://doi.org/10.1144/SP520-2021-50

Gale, A., Dalton, C. A., Langmuir, C. H., Su, Y., & Schilling, J.-G. (2013). The mean composition of ocean ridge basalts. *Geochemistry, Geophysics, Geosystems*, *14*(3), 489–518. https://doi.org/10.1029/2012GC004334

GEBCO Compilation Group. (2024). *GEBCO 2024 Grid*. Distributed by OpenTopography. https://doi.org/10.5069/G9D21VTT

Global Volcanism Program (Version v.5.2.7). (2024). Tofua Volcanic Arc in [Database] volcanoes of the World distributed by Smithsonian Institution, compiled by Venzke, E [Dataset]. https://doi.org/10.5479/si.GVP.VOTW5-2024.5.2

González-Vega, A., Callery, I., Arrieta, J. M., Santana-Casiano, J. M., Domínguez-Yanes, J. F., & Fraile-Nuez, E. (2022). Severe deoxygenation event caused by the 2011 eruption of the Submarine Volcano Tagoro (El Hierro, canary islands). *Frontiers in Marine Science*, *9*. https://doi.org/10.3389/fmars.2022.834691

Gupta, A. K., Bennartz, R., Fauria, K. E., & Mittal, T. (2022). Eruption chronology of the December 2021 to January 2022 Hunga Tonga-Hunga Ha'apai eruption sequence. *Communications Earth & Environment*, *3*(1), 1–10. https://doi.org/10.1038/s43247-022-00606-3

Hawkins, J. W. (1995). Evolution of the Lau Basin—Insights from ODP Leg 135. In *Active margins and marginal basins of the western Pacific* (pp. 125–173). American Geophysical Union (AGU). https://doi.org/10.1029/GM088p0125

Hayward, B. W., Sabaa, A. T., Howarth, J. D., Orpin, A. R., Strachan, L. J., & Tickle, S. E. (2022). Foraminiferal insights into the complexities of the turbidity currents triggered by the 2016 Kaikoura Earthquake, New Zealand. *Marine Micropaleontology*, *176*, 102171. https://doi.org/10.1016/j.marmicro.2022.102171

Hodkinson, R. A., & Cronan, D. S. (1998). Hydrothermal inputs at ODP sites 836, 837, 838 and 839 in relation to eastern Lau spreading Centre propagation in the Lau Basin, Southwest Pacific. *Geological Society, London, Special Publications*, *131*(1), 231–242. https://doi.org/10.1144/GSL.SP.1998.131.01.15

Horwell, C. J. (2007). Grain-size analysis of volcanic ash for the rapid assessment of respiratory health hazard. *Journal of Environmental Monitoring*, *9*(10), 1107–1115. https://doi.org/10.1039/B710583P

Hourdez, S., & Jollivet, D. (2018). CHUBACARC. End of cruise report. https://doi.org/10.13155/94968

Jutzeler, M., Marsh, R., Carey, R. J., White, J. D. L., Talling, P. J., & Karlstrom, L. (2014). On the fate of pumice rafts formed during the 2012 Havre submarine eruption. *Nature Communications*, *5*(1), 3660. https://doi.org/10.1038/ncomms4660

Kelly, L. J., Fauria, K. E., Manga, M., Cronin, S. J., Latu'ila, F. H., Paredes-Mariño, J., et al. (2024). Airfall volume of the 15 January 2022 eruption of Hunga volcano estimated from ocean color changes. *Bulletin of Volcanology*, *86*(6), 59. https://doi.org/10.1007/s00445-024-01744-6

Kennett, J. P., & Srinivasan, M. S. (1983). Neogene planktonic foraminifera: A phylogenetic atlas. Hutchinson Ross; Distributed by worldwide by Van Nostrand Reinhold.

Kneller, B. C., & Branney, M. J. (1995). Sustained high-density turbidity currents and the deposition of thick massive sands. *Sedimentology*, *42*(4), 607–616. https://doi.org/10.1111/j.1365-3091.1995.tb00395.x

Kranck, K. (1984). Grain-size characteristics of turbidites. *Geological Society, London, Special Publications*, *15*(1), 83–92. https://doi.org/10.1144/GSL.SP.1984.015.01.05

Le, J., & Shackleton, N. J. (1992). Carbonate dissolution fluctuations in the western equatorial Pacific during the late quaternary. *Paleoceanography*, *7*(1), 21–42. https://doi.org/10.1029/91PA02854

Ledbetter, M. T., & Sparks, R. S. J. (1979). Duration of large-magnitude explosive eruptions deduced from graded bedding in deep-sea ash layers. *Geology*, *7*(5), 240–244. https://doi.org/10.1130/0091-7613(1979)7<240:DOLEED>2.0.CO;2

Legros, F. (2002). Can dispersive pressure cause Inverse grading in grain flows? *Journal of Sedimentary Research*, *72*(1), 166–170. https://doi.org/10.1306/041301720166

Lynett, P., McCann, M., Zhou, Z., Renteria, W., Borrero, J., Greer, D., et al. (2022). Diverse tsunamigenesis triggered by the Hunga Tonga-Hunga Ha'apai eruption. *Nature*, *609*(7928), 728–733. https://doi.org/10.1038/s41586-022-05170-6

Manville, V., & Wilson, C. J. N. (2004). Vertical density currents: A review of their potential role in the deposition and interpretation of deep-sea ash layers. *Journal of the Geological Society*, *161*(6), 947–958. https://doi.org/10.1144/0016-764903-067

Mastin, L. G., Van Eaton, A. R., & Cronin, S. J. (2024). Did steam boost the height and growth rate of the giant Hunga eruption plume? *Bulletin of Volcanology*, *86*(7), 64. https://doi.org/10.1007/s00445-024-01749-1

Matoza, R. S., Fee, D., Assink, J. D., Iezzi, A. M., Green, D. N., Kim, K., et al. (2022). Atmospheric waves and global seismoacoustic observations of the January 2022 Hunga eruption, Tonga. *Science*, *377*(6601), 95–100. https://doi.org/10.1126/science.abo7063

McBride, E. F., Shepherd, R. G., & Crawley, R. A. (1975). Origin of parallel, near-horizontal laminae by migration of bed forms in a small flume. *Journal of Sedimentary Research*, *45*(1), 132–139. https://doi.org/10.1306/212F6CE9-2B24-11D7-8648000102C1865D

Metz, D., Watts, A. B., Grevemeyer, I., Rodgers, M., & Paulatto, M. (2016). Ultra-long-range hydroacoustic observations of submarine volcanic activity at Monowai, Kermadec Arc. *Geophysical Research Letters*, *43*(4), 1529–1536. https://doi.org/10.1002/2015GL067259

Moorby, S. A. (1986). Lithology, colour, mineralogy, and geochemistry of marine sediments from the Lau Basin, Havre Trough and Tonga Kermadec Ridge/. *New Zealand Oceanographic Institute, Division of Marine and Freshwater Science, DSIR*.

Mottl, M. J., Seewald, J. S., Wheat, C. G., Tivey, M. K., Michael, P. J., Proskurowski, G., et al. (2011). Chemistry of hot springs along the eastern Lau spreading center. *Geochimica et Cosmochimica Acta*, *75*(4), 1013–1038. https://doi.org/10.1016/j.gca.2010.12.008

Ohno, Y., Iguchi, A., Ijima, M., Yasumoto, K., & Suzuki, A. (2022). Coastal ecological impacts from pumice rafts. *Scientific Reports*, *12*(1), 11187. https://doi.org/10.1038/s41598-022-14614-y

Olivé Abelló, A., Vinha, B., Machín, F., Zerbetto, F., Bakalis, E., & Fraile-Nuez, E. (2021). Analysis of volcanic thermohaline fluctuations of Tagoro Submarine Volcano (El Hierro island, canary islands, Spain). *Geosciences*, *11*(9), 374. Article 9. https://doi.org/10.3390/geosciences11090374

Pattan, J. N., Shane, P., & Banakar, V. K. (1999). New occurrence of Youngest Toba Tuff in abyssal sediments of the central Indian basin. *Marine Geology*, *155*(3), 243–248. https://doi.org/10.1016/S0025-3227(98)00160-1

Pattan, J. N., Shane, P., Pearce, N. J. G., Banakar, V. K., & Parthiban, G. (2001). An occurrence of ∼ 74 ka Youngest Toba tephra from the western Continental Margin of India. *Current Science*, *80*(10), 1322–1326.

Piper, D. W. (1978). Turbidite muds and silts on deepsea fans and abyssal plains. Sedimentation in Submarine Canyons, Fans, and Trenches.

Ponomareva, V., Portnyagin, M., & Davies, S. M. (2015). Tephra without borders: Far-reaching Clues into past explosive eruptions. *Frontiers in Earth Science*, *3*. https://doi.org/10.3389/feart.2015.00083

Pope, E. L., Talling, P. J., & Carter, L. (2017). Which earthquakes trigger damaging submarine mass movements: Insights from a global record of submarine cable breaks? *Marine Geology*, *384*, 131–146. https://doi.org/10.1016/j.margeo.2016.01.009

Pouchou, J.-L., & Pichoir, F. (1991). Quantitative analysis of homogeneous or stratified Microvolumes applying the model "PAP". In K. F. J. Heinrich & D. E. Newbury (Eds.), *Electron probe quantitation* (pp. 31–75). Springer US. https://doi.org/10.1007/978-1-4899-2617-3_4

Proud, S. R., Prata, A. T., & Schmauß, S. (2022). The January 2022 eruption of Hunga Tonga-Hunga Ha'apai volcano reached the mesosphere. *Science*, *378*(6619), 554–557. https://doi.org/10.1126/science.abo4076

Reich, V., Marchig, V., Sunkel, G., & Weiss, W. (1990). Hydrothermal and volcanic input in sediments of the Lau Back-arc Basin, S.W. Pacific. In *Geological evolution and hydrothermal activity in the Lau and North Fiji basins* (pp. 183–203). Southwest Pacific Ocean.

Resing, J. A., Rubin, K. H., Embley, R. W., Lupton, J. E., Baker, E. T., Dziak, R. P., et al. (2011). Active submarine eruption of boninite in the northeastern Lau Basin. *Nature Geoscience*, *4*(11), 799–806. https://doi.org/10.1038/ngeo1275

Riech, V., Marchig, V., Sunkel, G., & Weiss, W. (1990). Hydrothermal and volcanic input in sediments of the Lau Back-Arc Basin, SW Pacific: Results of SONNE Cruise SO-35. In *Geological evolution and hydrothermal activity in the Lau and North Fiji Basins* (Vol. 92, p. 660). Schweizerbart.

Ross, P.-S., Dürig, T., Comida, P. P., Lefebvre, N., White, J. D. L., Andronico, D., et al. (2021). Standardized analysis of juvenile pyroclasts in comparative studies of primary magma fragmentation; 1. Overview and workflow. *Bulletin of Volcanology*, *84*(1), 13. https://doi.org/10.1007/s00445-021-01516-6

Rubin, K. H., & Macdougall, J. D. (1989). Submarine magma degassing and explosive magmatism at MacDonald (Tamarii) seamount. *Nature*, *341*(6237), 50–52. https://doi.org/10.1038/341050a0

Ryan, W. B. F., Carbotte, S. M., Coplan, J., O'Hara, S., Melkonian, A., Arko, R., et al. (2009). Global Multi-Resolution Topography (GMRT) synthesis data set [Dataset]. *Geochemistry, Geophysics, Geosystems*, *10*(3). https://doi.org/10.1029/2008GC002332

Schmid, F., Kopp, H., Schnabel, M., Dannowski, A., Heyde, I., Riedel, M., et al. (2020). Crustal structure of the niuafo'ou microplate and fonualei rift and spreading center in the Northeastern Lau Basin, Southwestern Pacific. *Journal of Geophysical Research: Solid Earth*, *125*(6). https://doi.org/10.1029/2019jb019184

Seabrook, S., Mackay, K., Watson, S., Clare, M., Hunt, J., Yeo, I., et al. (2023). Pyroclastic density currents explain far-reaching and diverse seafloor impacts of the 2022 Hunga Tonga Hunga Ha'apai eruption. *Research Square*. https://doi.org/10.21203/rs.3.rs-2395332/v1

Sen, A., Becker, E. L., Podowski, E. L., Wickes, L., Ma, S., Mullaugh, K., et al. (2013). Hydrothermal vent chimney megafaunal communities on the eastern Lau spreading center and Valu Fa Ridge. *Deep Sea Research Part I: Oceanographic Research Papers*, *72*, 48–60. https://doi.org/10.1016/j.dsr.2012.11.003

Sen, A., Kim, S., Miller, A. J., Hovey, K. J., Hourdez, S., Luther III, G. W., & Fisher, C. R. (2016). Peripheral communities of the eastern Lau spreading center and Valu Fa Ridge: Community composition, temporal change and comparison to near-vent communities. *Marine Ecology*, *37*(3), 599–617. https://doi.org/10.1111/maec.12313

Sigurdsson, H. (2015). Introduction. In H. Sigurdsson (Ed.), *The Encyclopedia of volcanoes* (2nd ed., pp. 1–12). Academic Press. https://doi.org/10.1016/B978-0-12-385938-9.02001-0

Somoza, L., González, F. J., Barker, S. J., Madureira, P., Medialdea, T., de Ignacio, C., et al. (2017). Evolution of submarine eruptive activity during the 2011–2012 El Hierro event as documented by hydroacoustic images and remotely operated vehicle observations. *Geochemistry, Geophysics, Geosystems*, *18*(8), 3109–3137. https://doi.org/10.1002/2016GC006733

Sparks, R. S. J., & Huang, T. C. (1980). The volcanological significance of deep-sea ash layers associated with ignimbrites. *Geological Magazine*, *117*(5), 425–436. https://doi.org/10.1017/S0016756800028533

Stevenson, C., Talling, P., Masson, D., Sumner, E., Frenz, M., & Wynn, R. (2013). The spatial and temporal distribution of grain-size breaks in turbidites. *Sedimentology*, *61*(4), 1120–1156. https://doi.org/10.1111/sed.12091

Stewart, M. S., Hannington, M. D., Emberley, J., Baxter, A. T., Krätschell, A., Petersen, S., et al. (2022). A new geological map of the Lau Basin (southwestern Pacific Ocean) reveals crustal growth processes in arc-backarc systems. *Geosphere*, *18*(2), 910–943. https://doi.org/10.1130/GES02340.1

Stow, D., & Smillie, Z. (2020). Distinguishing between deep-water sediment facies: Turbidites, Contourites and hemipelagites. *Geosciences*, *10*(2), 68. https://doi.org/10.3390/geosciences10020068

Stow, D. A. V., & Bowen, A. J. (1978). Origin of lamination in deep sea, fine-grained sediments. *Nature*, *274*(5669), 324–328. https://doi.org/10.1038/274324a0

Stow, D. A. V., & Shanmugam, G. (1980). Sequence of structures in fine-grained turbidites: Comparison of recent deep-sea and ancient flysch sediments. *Sedimentary Geology*, *25*(1), 23–42. https://doi.org/10.1016/0037-0738(80)90052-4

Sulpis, O., Boudreau, B. P., Mucci, A., Jenkins, C., Trossman, D. S., Arbic, B. K., & Key, R. M. (2018). Current CaCO3 dissolution at the seafloor caused by anthropogenic CO2. *Proceedings of the National Academy of Sciences of the United States of America*, *115*(46), 11700–11705. https://doi.org/10.1073/pnas.1804250115

Sulpis, O., Lix, C., Mucci, A., & Boudreau, B. P. (2017). Calcite dissolution kinetics at the sediment-water interface in natural seawater. *Marine Chemistry*, *195*, 70–83. https://doi.org/10.1016/j.marchem.2017.06.005

Sylvester, Z., & Lowe, D. R. (2004). Textural trends in turbidites and slurry beds from the Oligocene flysch of the East Carpathians, Romania. *Sedimentology*, *51*(5), 945–972. https://doi.org/10.1111/j.1365-3091.2004.00653.x

Taddeucci, J., Scarlato, P., Montanaro, C., Cimarelli, C., Del Bello, E., Freda, C., et al. (2011). Aggregation-dominated ash settling from the Eyjafjallajökull volcanic cloud illuminated by field and laboratory high-speed imaging. *Geology*, *39*(9), 891–894. https://doi.org/10.1130/G32016.1

Takahashi, K., & Be, A. W. H. (1984). Planktonic foraminifera: Factors controlling sinking speeds. *Deep-Sea Research, Part A: Oceanographic Research Papers*, *31*(12), 1477–1500. https://doi.org/10.1016/0198-0149(84)90083-9

Takahashi, K., & Honjo, S. (1983). Radiolarian skeletons: Size, weight, sinking speed, and residence time in tropical pelagic oceans. *Deep-Sea Research, Part A: Oceanographic Research Papers*, *30*(5), 543–568. https://doi.org/10.1016/0198-0149(83)90088-2

Talling, P. J., Amy, L. A., & Wynn, R. B. (2007). New insight into the evolution of large-volume turbidity currents: Comparison of turbidite shape and previous modelling results. *Sedimentology*, *54*(4), 737–769. https://doi.org/10.1111/j.1365-3091.2007.00858.x

Talling, P. J., Masson, D. G., Sumner, E. J., & Malgesini, G. (2012). Subaqueous sediment density flows: Depositional processes and deposit types. *Sedimentology*, *59*(7), 1937–2003. https://doi.org/10.1111/j.1365-3091.2012.01353.x

Taylor, B., Zellmer, K., Martinez, F., & Goodliffe, A. (1996). Sea-floor spreading in the Lau back-arc basin. *Earth and Planetary Science Letters*, *144*(1), 35–40. https://doi.org/10.1016/0012-821X(96)00148-3

Tepp, G., & Dziak, R. P. (2021). The seismo-acoustics of submarine volcanic eruptions. *Journal of Geophysical Research: Solid Earth*, *126*(4), e2020JB020912. https://doi.org/10.1029/2020JB020912

Trofimovs, J., Sparks, R. S. J., & Talling, P. J. (2008). Anatomy of a submarine pyroclastic flow and associated turbidity current: July 2003 dome collapse, Soufrière Hills volcano, Montserrat, West Indies. *Sedimentology*, *55*(3), 617–634. https://doi.org/10.1111/j.1365-3091.2007.00914.x

Usami, K., Ikehara, K., Jenkins, R. G., & Ashi, J. (2017). Benthic foraminiferal evidence of deep-sea sediment transport by the 2011 Tohoku-oki earthquake and tsunami. *Marine Geology*, *384*, 214–224. https://doi.org/10.1016/j.margeo.2016.04.001

10.1029/2024GC011629

Van Eaton, A. R., Lapierre, J., Behnke, S. A., Vagasky, C., Schultz, C. J., Pavolonis, M., et al. (2023). Lightning rings and gravity waves: Insights into the giant eruption plume from Tonga's Hunga Volcano on 15 January 2022. *Geophysical Research Letters*, *50*(12), e2022GL102341. https://doi.org/10.1029/2022GL102341

Walker, S. L., Baker, E. T., Chadwick, W. W., Jr., Rubin, K. H., Baumberger, T., Lupton, J. E., et al. (2019). *Deep ash plumes signal ongoing or recent submarine volcanic eruptions, and demonstrate a syn-eruptive process for dispersing fine ash to distal sediments*. AGU Fall Meeting Abstracts. V43H-0185.

Wetzel, A. (2009). The preservation potential of ash layers in the deep-sea: The example of the 1991-Pinatubo ash in the South China Sea. *Sedimentology*, *56*(7), 1992–2009. https://doi.org/10.1111/j.1365-3091.2009.01066.x

White, J. D. L., Schipper, C. I., & Kano, K. (2015). Chapter 31—Submarine explosive eruptions. In H. Sigurdsson (Ed.), *The Encyclopedia of volcanoes* (2nd ed., pp. 553–569). Academic Press. https://doi.org/10.1016/B978-0-12-385938-9.00031-6

Whiteside, A., Dupouy, C., Singh, A., Bani, P., Tan, J., & Frouin, R. (2023). Impact of ashes from the 2022 Tonga volcanic eruption on satellite ocean color signatures. *Frontiers in Marine Science*, *9*. https://doi.org/10.3389/fmars.2022.1028022

Wiesner, M. G., Wang, Y., & Zheng, L. (1995). Fallout of volcanic ash to the deep South China Sea induced by the 1991 eruption of Mount Pinatubo (Philippines). *Geology*, *23*(10), 885–888. https://doi.org/10.1130/0091-7613(1995)023<0885:FOVATT>2.3.CO;2

Yan, Q., Straub, S., Castillo, P., Zhang, H., Tian, L., & Shi, X. (2020). Hafnium isotope constraints on the nature of the mantle beneath the Southern Lau basin (SW Pacific). *Scientific Reports*, *10*(1), 17476. https://doi.org/10.1038/s41598-020-74565-0

Yoon, J.-E., King, D., Longman, J., & Cronin, S. J. (2023). Differential response of chlorophyll-a concentrations to explosive volcanism in the western South Pacific. *Frontiers in Marine Science*, *10*. https://doi.org/10.3389/fmars.2023.1072610